



Atomic coherence-state phase conjugation in optical coherent transients
by Zachary Cole

A thesis submitted in partial fulfillment of the requirements for the degree of Master of Science in
Physics

Montana State University

© Copyright by Zachary Cole (2000)

Abstract:

Atomic coherence-state phase conjugation is studied via optical coherent transient phenomena, in Tm^{3+} : YAG. The theoretical framework is a semi-classical perturbative approach to time-domain wave mixing in an inhomogeneously broadened two-level atomic system. Phase conjugation occurs between coherence-state pathways associated with the stimulated photon echo and the so-called 'virtual' echo. The pathway associated with the virtual echo is experimentally shown to exist for causal time domains through its coherence decay and optical processing relations to the stimulated photon echo pathway. A conjecture is presented which links phase conjugation to a correspondence symmetry between spatial and frequency holography.

ATOMIC COHERENCE-STATE PHASE CONJUGATION IN OPTICAL
COHERENT TRANSIENTS

by

Zachary Cole

A thesis submitted in partial fulfillment
of the requirements for the degree

of

Master of Science

in

Physics

MONTANA STATE UNIVERSITY-BOZEMAN
Bozeman, Montana

May 2000

N378
C6762

APPROVAL

of a thesis submitted by

Zachary Cole

This thesis has been read by each member of the thesis committee and has been found to be satisfactory regarding content, English usage, format, citations, bibliographic style, and consistency, and is ready for submission to the College of Graduate Studies.

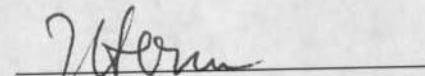
W. R. Babbitt, Ph. D


(Signature)

01/06/00
Date

Approved for the Department of Physics


John C. Hermanson, Ph. D


(Signature)

12-10-99
Date

Approved for the College of Graduate Studies

Bruce R. McLeod, Ph. D.


(Signature)

1-11-00
Date

STATEMENT OF PERMISSION TO USE

In presenting this thesis in partial fulfillment of the requirements for a master's degree at Montana State University-Bozeman, I agree that the Library shall make it available to borrowers under rules of the Library.

If I have indicated my intention to copyright this thesis by including a copyright notice page, copying is allowable only for scholarly purposes, consistent with "fair use" as prescribed in the U.S. Copyright Law. Requests for permission for extended quotation from or reproduction of this thesis in whole or in parts may be granted only by the copyright holder.

Signature Jacky Cole

Date 12-10-99

The scientist does not study nature because it is useful; he studies it because he delights in it, and he delights in it because it is beautiful.

– Henri Poincaré

ACKNOWLEDGMENTS

It is my pleasure to acknowledge the support and guidance I have received from Dr. William Randall Babbitt, who served as my advisor and mentor with uncanny distinction. Dr. Babbitt allowed me great freedom and encouragement in pursuing the topics which I found interesting and was an active participant in exploring those topics. I would also like to thank Dr. K. D. Merkel because without his in-depth laboratory knowledge and willingness to teach, the work presented in this thesis would still be in progress. In addition this work was born, in part, through many conversations with Dr. Alex Rebane.

Finally, I owe my partner, Jennieven Wyllys, more than words, in specific, dinners, back-rubs and an endless reservoir of support and encouragement, which she has given me.

TABLE OF CONTENTS

	Page
1. INTRODUCTION.....	1
Motivation.....	1
2. THEORY.....	4
Spatial Holography	4
Spatial-Spectral Holography	6
Spectral Broadening.....	7
Time-Domain Four Wave-Mixing.....	8
Pathologies of the Atomic Response	12
Double-sided Feynman Diagrams	13
Green Function Perturbative Expansion	20
Evolution.....	23
The Atomic Response in Time Domain Four-Wave Mixing.....	31
Correspondence.....	35
3. EXPERIMENTAL TECHNIQUES	36
Introduction.....	36
Six Wave-Mixing.....	37
Experiments	38
Experimental Set-Up	39
Material Considerations	40
Experiment I: 4WM and 6WM Signal Dependence on θ_4	41
Experiment II: 6WM with Variable τ_{21}	46
Experiment III: 6WM with 5-Bit Bi-Phase Barker Codes.....	49
4. SUMMARY	52
REFERENCES CITED.....	53

LIST OF FIGURES

Figure 2.1: The interference between object and reference waveforms is recorded in the holographic medium.	4
Figure 2.2: Illumination of the hologram at a later time by a 'recall' beam (identical to the reference beam) results in two first-order diffracted waveforms.	6
Figure 2.3: Individual absorbers experience slightly different lattice environments resulting in a shift of their resonant energy (above). The overall effect is an inhomogeneous broadening (below).	7
Figure 2.4: A possible time-domain four-wave mixing input scheme for a stimulated photon echo experiment. The detector is placed according to the spatial phase-matching conditions.	9
Figure 2.5: Time domain four-wave mixing and corresponding coherence-state phase evolution.	11
Figure 2.6: Interaction of the density operator with perturbative waveforms is graphically depicted by double-sided Feynman diagrams.	14
Figure 2.7: The double-sided Feynman diagrams for a first order perturbation.	15
Figure 2.8: The double-sided Feynman diagrams for a second time orderd perturbation.	16

Figure 2.9: The double-sided Feynman diagrams for time domain four-wave mixing. The eight diagrams of Figures 2.8 and 2.9 create conjugate half spaces labeled R1-R4 and R*1-R*4.	17
Figure 2.10: The double-sided Feynman diagrams for time domain four-wave mixing. The eight diagrams of Figures 2.8 and 2.9 create conjugate half spaces labeled R1-R4 and R*1-R*4.	18
Figure 2.11: An optical waveform interacting with a two level atomic system.	19
Figure 2.12: Time-domain 4WM input sequence with corresponding coherence-state phase evolution.	30
Figure 2.13: The double-sided Feynman diagrams of time-domain four wave-mixing (SPE contribution).	34
Figure 3.1: The six wave-mixing technique used to rephase all four wave-mixing coherence-state paths.	37
Figure 3.2: Six wave-mixing experimental apparatus.	39
Figure 3.3: The expected four and six wave-mixing signals generated from the 6WM input scheme.	42
Figure 3.4: Six wave-mixing with variable θ_4	43
Figure 3.5: Six wave-mixing with variable θ_4 . Signal attenuation of the R-SPE, PE _(E3, E4) and R-VE with decreasing θ_4	44
Figure 3.6: Six wave-mixing with variable θ_4 . The SPE _(E1, E2, E4) response to decreasing θ_4	45

Figure 3.7: Captured signals for 6WM with variable τ_{21}	47
Figure 3.8: Power of R-SPE and R-VE versus τ_{21} , along with theoretical fits.....	48
Figure 3.9: Six-wave mixing with the 5b-bc (4WM signals ignored).	51
Figure 3.10: Captured signals of 6WM with 5b-bc:	51

ABSTRACT

Atomic coherence-state phase conjugation is studied via optical coherent transient phenomena, in Tm^{+3} : YAG. The theoretical framework is a semi-classical perturbative approach to time-domain wave mixing in an inhomogeneously broadened two-level atomic system. Phase conjugation occurs between coherence-state pathways associated with the stimulated photon echo and the so-called 'virtual' echo. The pathway associated with the virtual echo is experimentally shown to exist for causal time domains through its coherence decay and optical processing relations to the stimulated photon echo pathway. A conjecture is presented which links phase conjugation to a correspondence symmetry between spatial and frequency holography.

CHAPTER 1

INTRODUCTION

The investigation of resonant interactions between light and matter has illuminated dynamics which make it possible to store and process the spectral (energetic) character of light in a crystalline environment¹⁻⁹. This is achieved through a quantum mechanical analog to traditional spatial holography, known as spatial-spectral holography (S-S-H), or time and space domain holography. The spectral information of a coherent 'object' light pulse is stored in the absorption spectrum of an inhomogeneously broadened two-level atomic system (IBA) by interfering it with a brief 'reference' pulse inside the medium. A spatial-spectral population grating ensues, which may be illuminated at a later time by a brief 'recall' pulse. The recall pulse stimulates a coherence-state evolution that emits a time-domain replica of the object pulse. This spatial-spectral holographic event is known as the stimulated photon echo (SPE)

Motivation

In the mathematical formulation where the SPE is considered an optical coherent transient (OCT), the coherence-state stimulated by the recall pulse contains multiple terms that are conjugate in their phase evolution. These terms correspond to pathways of

the medium's response to waveform perturbations. One set of the coherence state pathways corresponds to the SPE event, while the other set appears to promote an echo event prior to the recall pulse, known as the 'virtual' echo (VE). The VE, being a non-causal event, does not exist. This set of coherence-state paths, called here the virtual coherence (VC), was first postulated in spin echo studies of magnetic resonance phenomena¹⁰.

Although the VE does not exist, the research presented in this thesis indicates that after pulse 3, the medium evolves in every way as if the virtual echo had occurred.

A quantified relationship between the phase conjugate sets of coherence state pathways has, we believe until now, not been demonstrated in a solid material. In an aqueous medium it is possible to heterodyne (phase) detect portions of both the SPE and VE¹¹. However, these methods are fundamentally limited in their ability to detect full echo events associated with the conjugate coherence-state pathways and are not in general applicable to a solid-state medium¹².

In this study, echoes resulting from the conjugate paths are recorded and characterized in a crystal lattice environment. Unlike the measurements of reference [11], fully rephased stimulated echo signals are detected. This is achieved through a six wave-mixing technique that introduces another pulse into the medium after the SPE. This has the effect of inverting the phase evolution of the coherence-state pathways such that echo signals associated with all pathways are produced. The conjugate pathways are characterized through their six-wave mixing signals.

The organization of this thesis is as follows: in chapter 2, theoretical considerations, beginning with a general overview of spatial and spatial-spectral holography, are introduced. The remainder of chapter 2 develops time-domain four-wave mixing theory (TD4WM). This approach illuminates the multiple pathways of the medium's response to optical waveform interaction. Experimental techniques and considerations are presented in chapter 3 along with results. Chapter 4 concludes the thesis.

CHAPTER 2

THEORY

Spatial Holography

In classical (spatial) thin film holography, the interference pattern of two beams (object and reference), is recorded in the absorption spectrum of a holographic medium¹³ (see Figure 2.1).

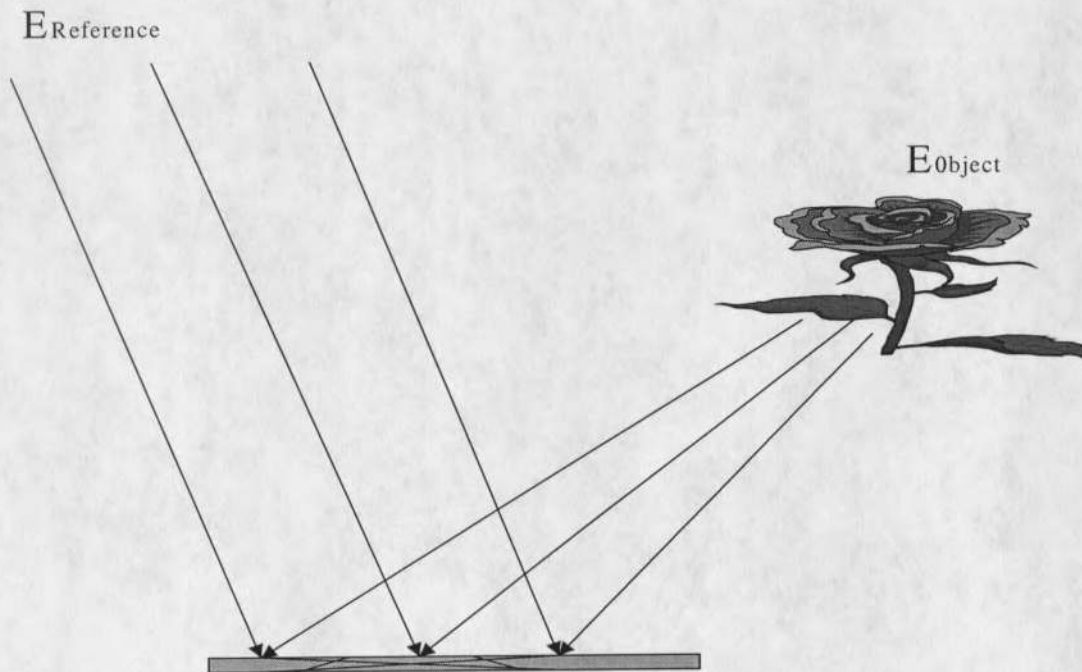


Figure 2.1: The interference between object and reference waveforms is recorded in the holographic medium.

The primary distinction between holography and photography is that the hologram is able to spatially store the phase relationship between the two beams. The interference pattern is stored in the intensity profile of the medium. In complex notation the interference terms of the intensity profile are conjugate in phase, ensuring that the intensity and recorded interference grating is real:

$$\begin{aligned} \text{Intensity} &= \left| E_{\text{reference}} + E_{\text{object}} \right|^2 \\ &= E_r^2 + E_o^2 + E_r E_o e^{i\varphi_{\text{relative}}(\mathbf{r})} + E_r E_o e^{-i\varphi_{\text{relative}}(\mathbf{r})} \end{aligned} \quad (1)$$

The holographic images are formed by scattering a third 'recall' beam (identical to the reference beam) through the medium. This beam will scatter into two first order waveforms representing a recreation of the object wave and a wavefront that is phase conjugate to the object.

The electric field amplitude of the output may be expressed as:

$$\begin{aligned} \text{Transmission} &\propto [\text{non-diffracted terms}] \\ &+ E_r^2 E_o e^{i\varphi_o(\mathbf{r}_o)} + E_r^2 E_o e^{-i\varphi_o(\mathbf{r}_o)} e^{i2\varphi_r(\mathbf{r}_r)} \end{aligned} \quad (2)$$

Equation (2) assumes that $E_{\text{recall}} = E_{\text{reference}} = E_r e^{i\varphi_r(\mathbf{r}_r)}$. The two diffracted terms of Equation (2) are phase conjugate with respect to the object wavefront. The scattered waveforms are known as the real and virtual image. The virtual image spatially diverges away from the hologram, appearing to converge behind the scattering center. The real image converges to produce an inverted (pseudoscopic) recreation of the object wavefront, as depicted in Figure 2.2.

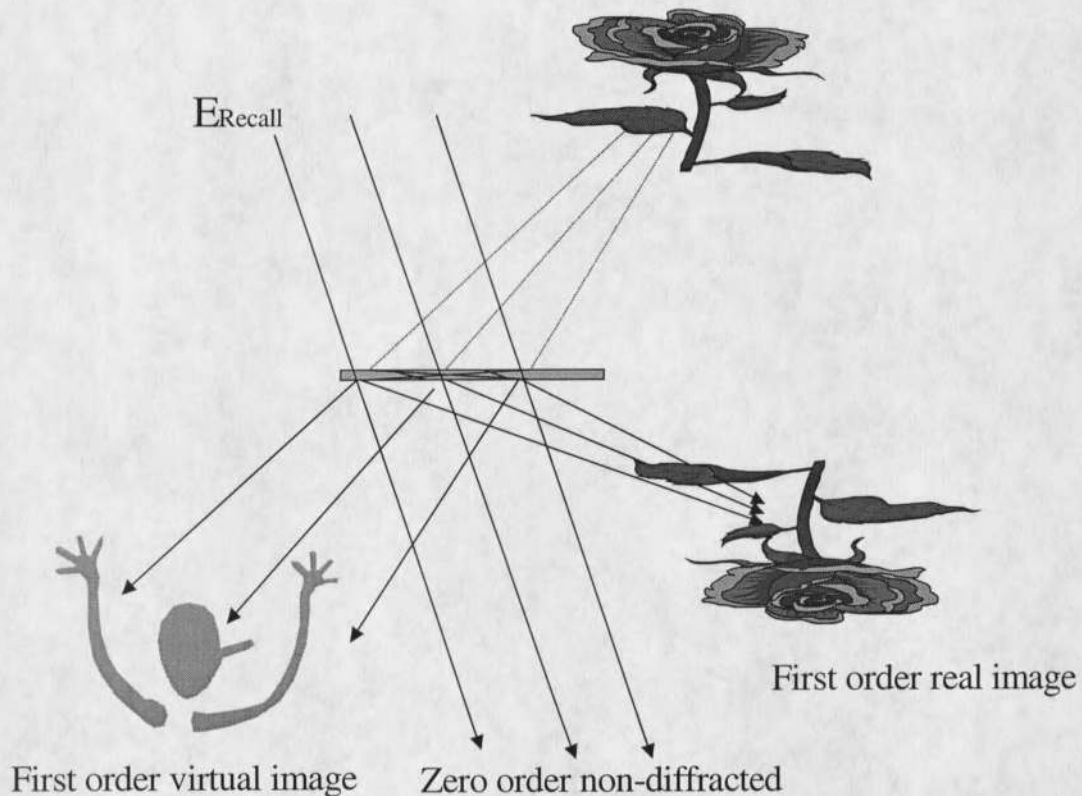


Figure 2.2: Illumination of the hologram at a later time by a 'recall' beam (identical to the reference beam) results in two first-order diffracted waveforms.

Spatial-Spectral Holography

In spatial-spectral holography (SSH), also known as time and space domain holography, the interference of object and reference pulsed waveforms is recorded as a frequency dependent absorption spectrum of the spectral holographic medium. This is achieved by separating the object and reference pulses in time by a delay, τ_{21} . At a later time, a 'recall' pulse interacts with the spatial-spectral holographic grating and a reproduction of the object pulse is emitted, τ_{21} later. The delayed waveform is known as the stimulated photon echo (SPE). The time delay behavior of the echo event is related to

the spatial-spectral holographic medium being inhomogeneously broadened in its electronic absorption spectrum.

Spectral Broadening

A crystal lattice, having defects and irregularities, provides slightly different electronic potential environments to the active guest ions, serving to statically perturb their electronic energy states. The ensemble of dopant ions then have a spectral absorption profile broader than the 'natural' homogenous profile of a single ion embedded in an ideal matrix. The system is then inhomogeneously broadened as depicted in Figure 2.3.

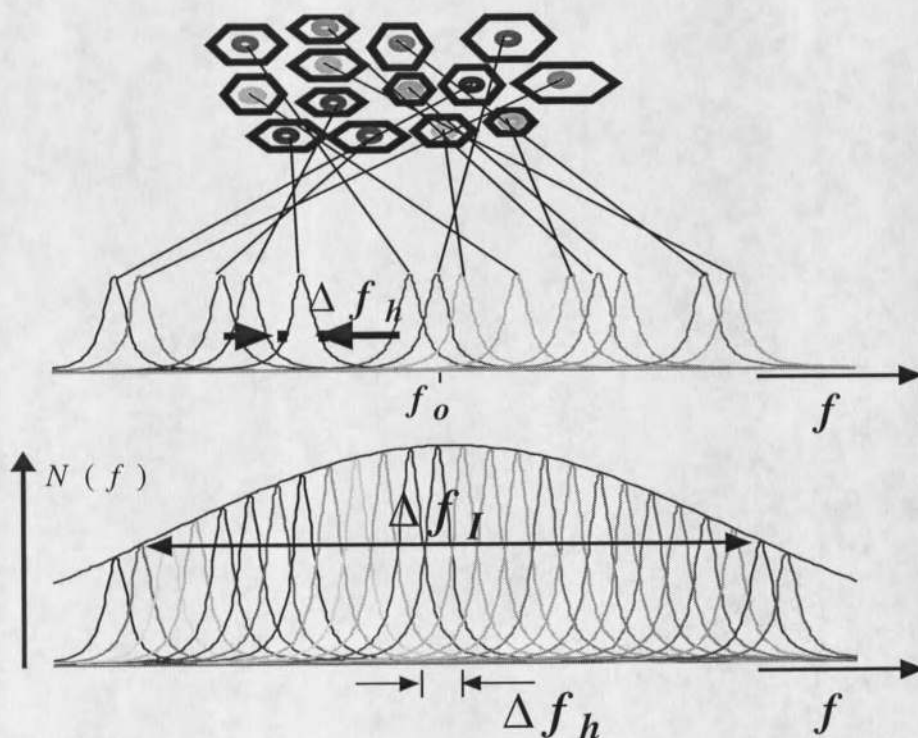


Figure 2.3: Individual absorbers experience slightly different lattice environments resulting in a shift of their resonant energy (above). The overall effect is an inhomogeneous broadening (below).

Due to the random nature of the inhomogeneous broadening, the absorption profile is modeled as a Gaussian distribution with linewidth Δf_I , whereas the homogenous profile, due to dynamic perturbations and uncertainty, is modeled as a Lorentzian distribution with linewidth Δf_H .

Both the static inhomogeneous broadening and the dynamic homogenous broadening contribute to the SPE event, but in very different ways. The homogenous contribution promotes irreversible dynamic relaxation processes and will be considered in Chapter 3. The inhomogeneous broadening promotes coherence-state dephasing (inhomogeneous dephasing) between the various frequency components of the object pulse. This inhomogeneous dephasing is crucial to the time-delayed behavior of the spatial-spectral holography. In order to understand how inhomogeneous broadening is responsible for the time delay of the echo, we view the entire process as time-domain four-wave mixing.

Time-Domain Four Wave-Mixing

The time-domain four wave-mixing process of this work introduces 3 input waveforms to interact with a nonlinear medium, which then emits a new field, the response of the system. The SPE is one such time-domain four-wave mixing (4WM) signal. A typical input scheme in a SPE experiment consists of three temporally unique, angled pulses spatially overlapping in an interaction volume of the IBA. (see Figure 2.4).

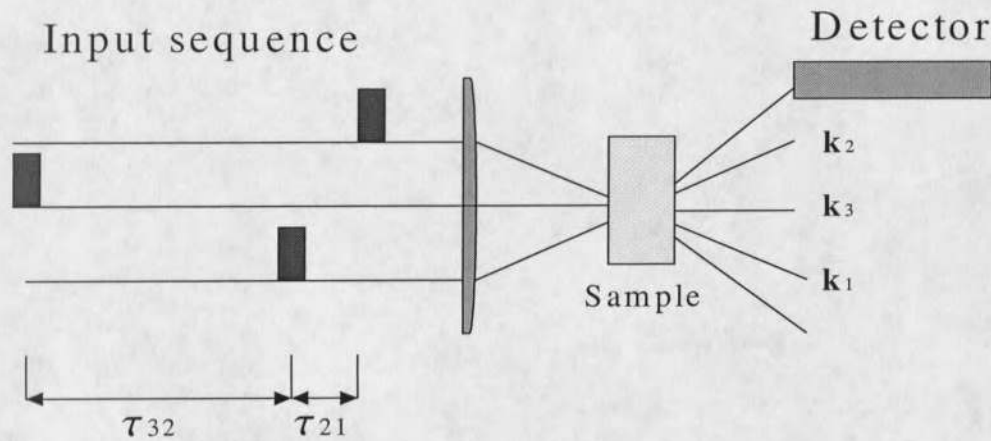


Figure 2.4: A possible time-domain four-wave mixing input scheme for a stimulated photon echo experiment. The detector is placed according to the spatial phase-matching conditions.

The first two input pulses, with wave vectors \mathbf{k}_1 and \mathbf{k}_2 respectively, interfere in the IBA causing a spatial and frequency dependant absorption grating with period $1/\tau_{21}$, where τ_{21} is the temporal delay between pulse one and two. Pulse 1 creates a coherence-state in the medium. The Fourier limited energy spectrum of pulse 1 interacts resonantly with the inhomogeneously broadened dopant ions of the IBA. The homogeneous frequency components of the coherence-state have an oscillating phase evolution with frequency proportional to their resonant transition. Because of this, the inhomogeneously broadened ensemble undergoes relative dephasing, called inhomogeneous dephasing. The reference pulse then takes the inhomogeneously dephased coherence-state and converts it to a spatial-spectral population grating at τ_{21} after pulse 1. The delay τ_{21} , must be less than the dephasing relaxation parameter, $T_2 = 1/2\pi\Delta f_H$ (i.e. the characteristic time in which the coherence state loses its well-defined phase relation due to dynamic

(homogeneous) relaxation processes and greater than the inverse inhomogeneous linewidth, $\tau_{21} > 1/\Delta f_1^{14}$. The spatial-spectral grating now contains information about the interference pattern (including time delay) of the two pulses, stored in the power spectrum of the IBA, given as:

$$\rho_{ee}(f) \propto |E_1(f)|^2 + |E_2(f)|^2 + E_1^*(f)E_2(f)e^{-2\pi if\tau_{21}} + E_1(f)E_2^*(f)e^{2\pi if\tau_{21}}, \quad (3)$$

where ρ is the density operator (see reference [15] for a detailed discussion of the density operator.).

The persistence of the grating depends upon the upper state lifetime of the medium, known as T_1 (assuming other grating decay mechanisms are ignored).

A third pulse is then introduced at time $t_3 < T_1$. This pulse stimulates an evolving coherence state from the spatial-spectral grating that is in the process of inhomogeneous rephasing. The effect of the inhomogeneous dephasing that occurred during the first time period is eliminated by the inhomogeneous rephasing at τ_{21} after pulse 3. This means the inhomogeneously evolving atomic coherence-state then has its relative phase equal to zero and the SPE is emitted, so long as the input wave vectors satisfy spatial phase matching conditions.

The third pulse also stimulates another set of coherence-state pathways. These pathways continue the process of inhomogeneous dephasing, established during the first time period, such that if time were run in reverse they would re-phase at τ_{21} before pulse three. This set of pathways is associated with the previously mentioned virtual echo and does not in general contribute to an echo signal. However, as will be shown in the following sections, there is no violation of causality in this description. The two sets of

coherence-state pathways are phase conjugate to each other in their evolution as depicted in Figure 2.5.

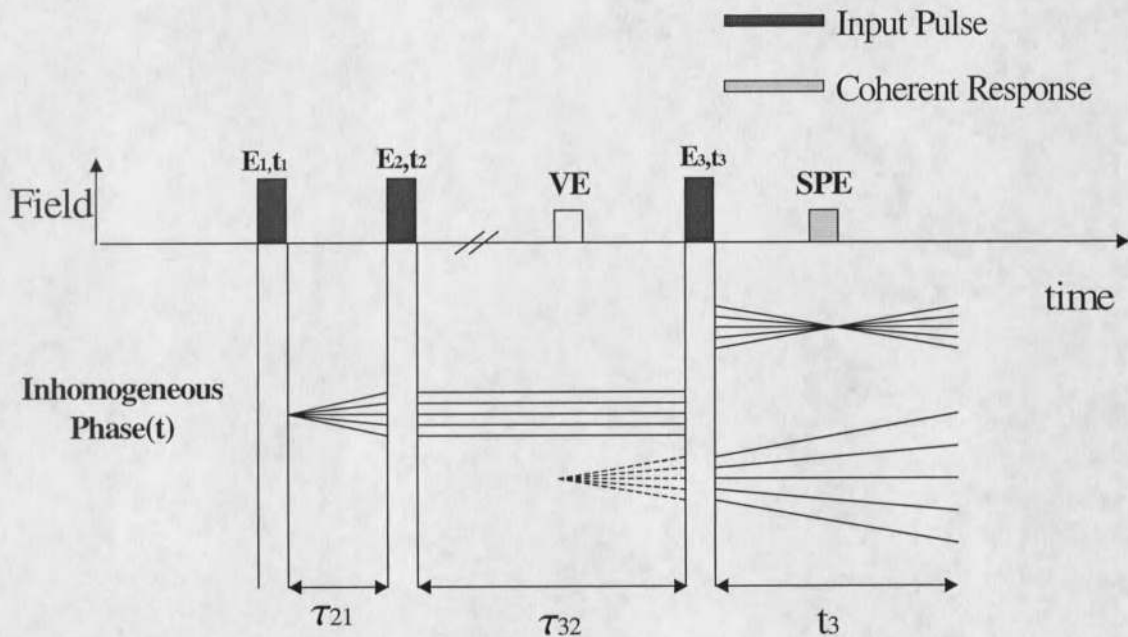


Figure 2.5: Time domain four-wave mixing and corresponding coherence-state phase evolution.

The temporal delay in spatial-spectral holography introduced as a variant from spatial holography establishes a temporal rephasing condition on the SPE event through the inhomogeneous broadening mechanism (i.e. an echo occurs only when a coherence state evolves in a rephasing manner).

In order to mathematically understand the conjugate nature of the coherent-state pathways associated with the SPE and VE, we review time domain 4WM in terms of atomic response function theory (see reference [16] for an extensive overview of response function theory).

Pathways of the Atomic Response

Consider a two-level atomic system with excited electronic eigenstate $|e\rangle$, and ground state $|g\rangle$. The atomic density operator may be expanded in this basis as:

$$\rho(t) = \sum_{\substack{n=e,g \\ m=e,g}} \rho_{n,m}(t) |n\rangle\langle m|, \quad (4)$$

In its matrix form,

$$\rho(t) = \begin{bmatrix} \rho_{gg}(t) & \rho_{ge}(t) \\ \rho_{eg}(t) & \rho_{ee}(t) \end{bmatrix}, \quad (5)$$

the diagonal terms represent populations and the off diagonal represent coherence-states of the system. The density operator is Hermitian, i.e, $\rho_{eg}(t) = \rho_{ge}^*(t)$, or in terms of static operator notation, $|e\rangle\langle g| = [|g\rangle\langle e|]^\dagger$.

In quantum mechanics observables have real eigenvalues and are expressed by Hermitian operators. The use of complex numbers in QM is seen to be an essential feature of the theory¹⁷. In this section it will be shown that the Hermitian condition forces the system into pathways and in the next section it will be shown that in order to describe the system in full, all paths must be accounted for.

In this section, we will graphically depict how a first order waveform statically effects the two level system. The following sections will address the dynamic time evolution.

The electric field takes the form:

$$E(\mathbf{r}, t) = \varepsilon(t) \exp[i(\mathbf{k} \cdot \mathbf{x} - \omega t)] + \varepsilon^*(t) \exp[-i(\mathbf{k} \cdot \mathbf{x} - \omega t)]. \quad (6)$$

A first order perturbation may take a small portion of the population and create a coherence-state or convert a small coherence state into a population (i.e. in equation (5) diagonal element \rightarrow off - diagonal, and vice versa). If the state is initially pure:

$$\rho_0 = \rho_{gg} = |g\rangle\langle g|. \quad (7)$$

It can be perturbed into

$$\rho_{ge} = |g\rangle\langle e|. \quad (8)$$

or

$$\rho_{eg} = |e\rangle\langle g|. \quad (9)$$

The two Hermitian conjugate coherence-states of equations (8) and (9), can be viewed as resulting from the perturbing waveform interacting with the density operator. This interaction is diagrammatically expressed with the double-sided Feynman diagrams^{12, 16}. The utility of these diagrams is in viewing the pathways in which the system may evolve.

Double-sided Feynman Diagrams

When an electric field envelope expressed in complex notation perturbs the Hermitian operator, ρ , the effects may be graphically depicted. In Figure 2.4, two parallel lines together represent the ket-bra description of the static portion of the density operator. An arrow intersecting one of the lines at a given time represents a time ordered

interaction with the radiation field. At this point, dynamic evolution of the system is not addressed, simply the static effects of the interactions.

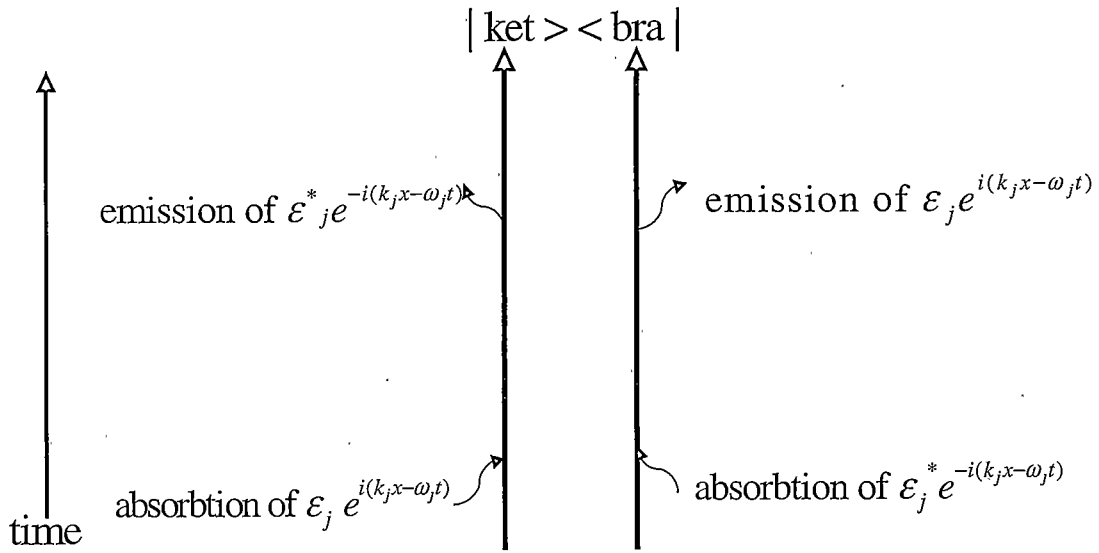


Figure 2.6: Interaction of the density operator with perturbative waveforms is graphically depicted by double-sided Feynman diagrams.

In Figure 2.6, an arrow pointing right constitutes an interaction with $\epsilon_j e^{(-i\omega_j t + i\vec{k}_j \cdot \vec{r})}$, and an arrow pointing left is a contribution from its conjugate, $\epsilon_j^* e^{(i\omega_j t - i\vec{k}_j \cdot \vec{r})}$. Arrows pointing into (out of) the diagram represent stimulated photon absorption (emission).

This graphical description will be followed through three temporally isolated perturbations so as to view the nature of the pathways that the system undergoes in a typical SPE experiment. A more rigorous treatment of the pathways and how the echo phenomenon occurs will be given in the following sections.

The effects of the first waveform perturbation on the ground state system is diagrammatically expressed in Figure 2.7.

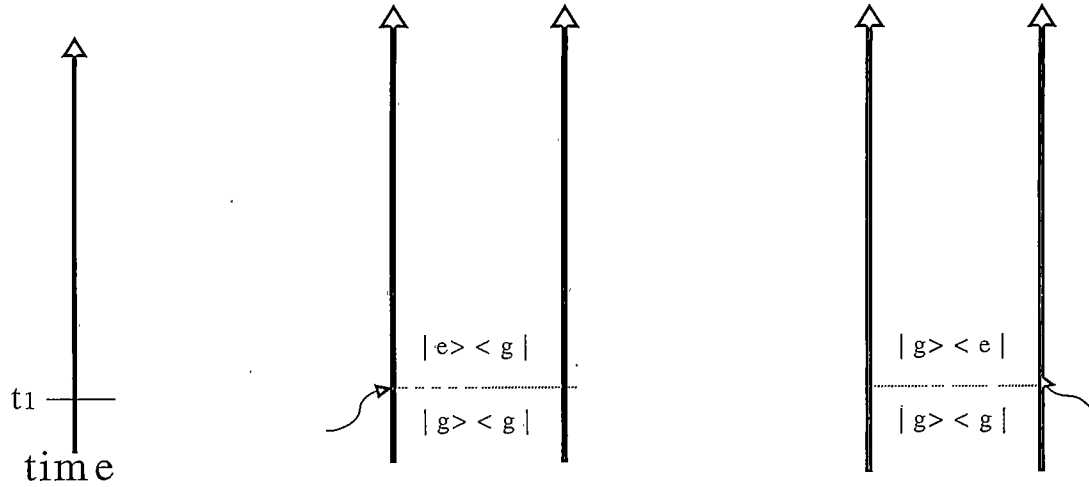


Figure 2.7: The double-sided Feynman diagrams for a first order perturbation.

The two diagrams in Figure 2.6 represent the system being perturbed from an initial ground population state, into both an excited-ground ($\rho_{eg} = |e\rangle\langle g|$) and ground-excited ($\rho_{ge} = |g\rangle\langle e|$) coherence state. This occurs due to the absorption of $\varepsilon_j e^{(-i\omega_j t + i\vec{k}_j \cdot \vec{r})}$ by the ket and the absorption of $\varepsilon_j^* e^{(i\omega_j t - i\vec{k}_j \cdot \vec{r})}$ by the bra. In a statistical interpretation of quantum mechanics both paths are taken.

We note that there is the possibility for ω_j to combine with the resonant transition of the medium, ω_{eg} , in a highly oscillatory manner. In this case, it would be possible for the absorption (emission) of a photon corresponding to a transition from the excited to ground (ground to excited) electronic states. Here, we are only considering the resonant

effects and ignore this highly oscillatory contribution. This is the so-called rotating wave approximation (RWA).

When the system is perturbed by another waveform at time t_2 , both diagrams of Figure 2.7 again have multiple paths. The waveform may affect both the bra and the ket portions of the system, giving rise to either absorption or emission of a photon, which results in the coherence-states being converted into populations. In this description, the system is considered to follow both pathways, so in general the two diagrams of Figure 2.7 each contribute to an excited state grating ($\rho_{ee} = |e\rangle\langle e|$) and a ground state grating ($\rho_{gg} = |g\rangle\langle g|$) as shown in Figure 2.8.

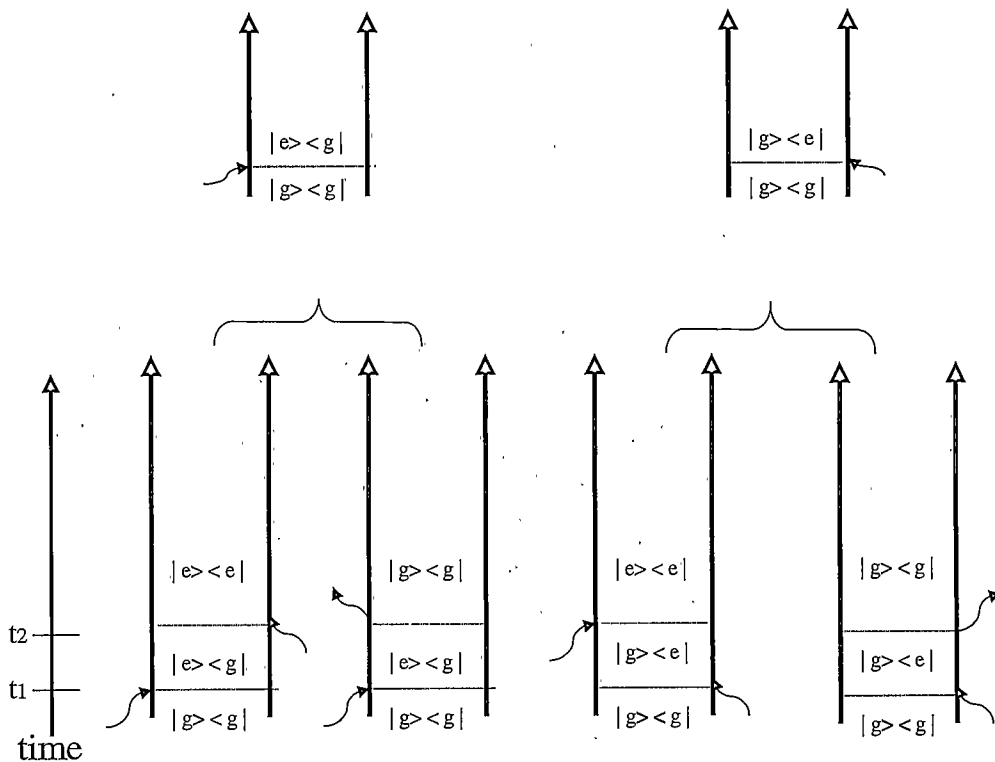


Figure 2.8: The double-sided Feynman diagrams for a second time order perturbation.

Following the same reasoning, each of the four pathways of Figure 2.8 will bifurcate again when the system interacts with another pulse at time t_3 (see Figure 2.9 and Figure 2.10). This process is identical to the initial perturbation depicted in Figure 2.7. These eight diagrams represent the pathways of the atomic system in a time-domain four-wave mixing process.

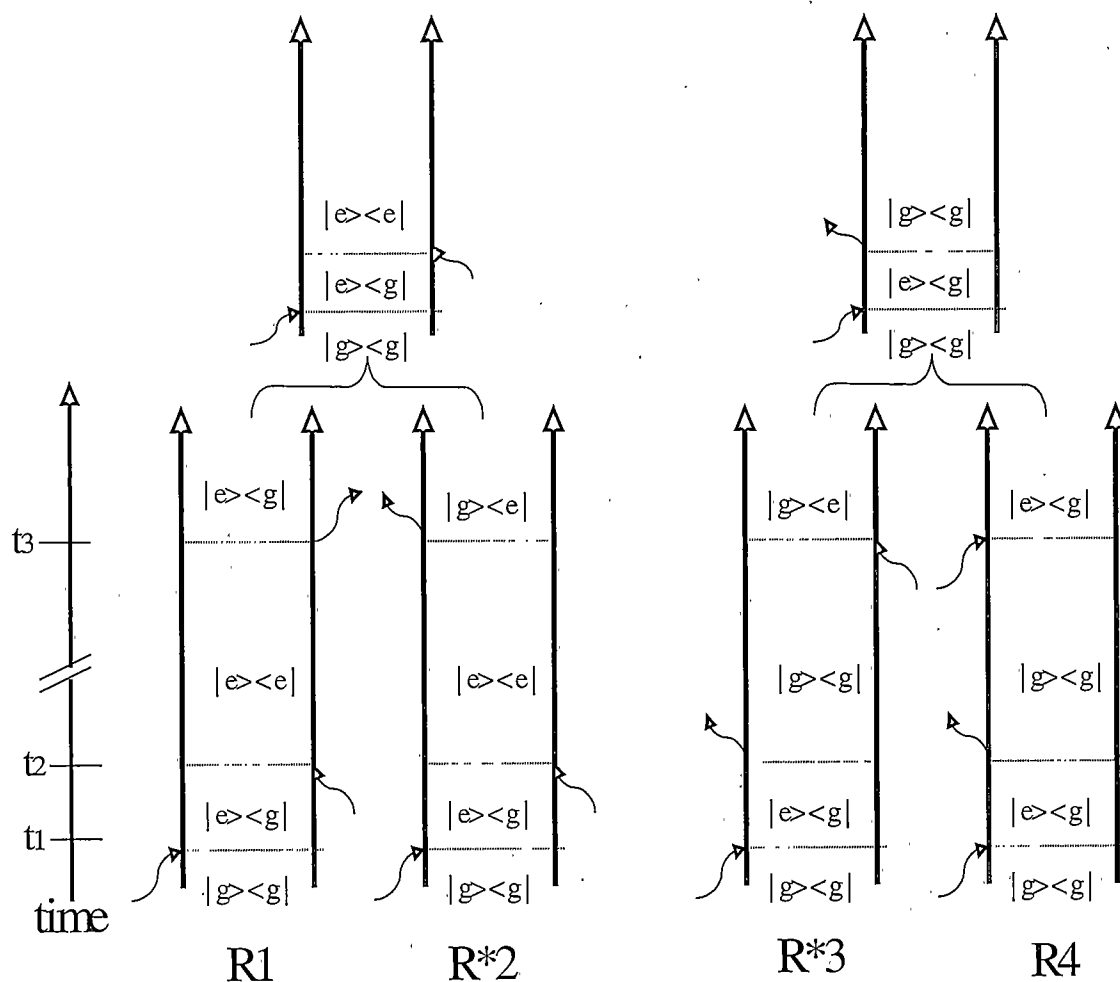


Figure 2.9: The double-sided Feynman diagrams for time domain four-wave mixing. The eight diagrams of Figures 2.8 and 2.9 create conjugate half spaces labeled R1-R4 and R*1-R*4.

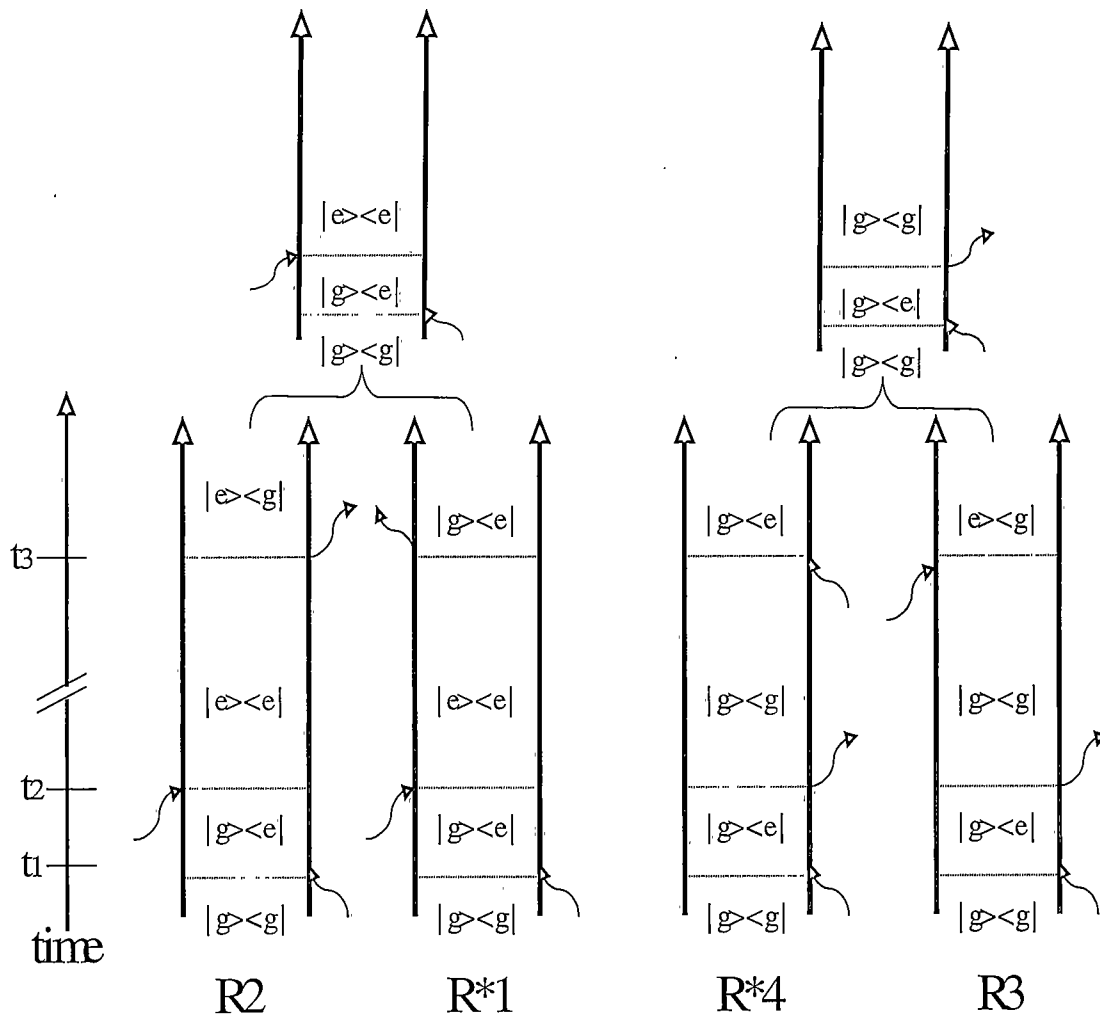


Figure 2.10: The double-sided Feynman diagrams for time domain four-wave mixing. The eight diagrams of Figures 2.8 and 2.9 create conjugate half spaces labeled R1-R4 and R*1-R*4.

The double-sided Feynman diagrams for time-domain four-wave mixing in a two level system are labeled with R values because, as will be shown in the next section, they are graphic representations of the atomic response functions. The eight diagrams R1-R4 and R*1-R*4 express the entire response and create conjugate half-spaces. This is seen by flipping R1-R4 diagrams about a vertical axis, replicating the R*1-R*4 pathways;

effectively switching every interaction with $\varepsilon_j e^{(-i\omega_j t + i\vec{k}_j \cdot \vec{r})}$ to $\varepsilon_j^* e^{(i\omega_j t - i\vec{k}_j \cdot \vec{r})}$ and vice versa, for a given diagram.

The diagrams also give the phase matching, frequency mixing, and field envelope terms of the 4WM signal. The arrows for each pathway relate such information by reading off the sequence of waveform contributions. For example, R2 and R3 have contributions from $\varepsilon_1^* e^{(i\omega_1 t - i\vec{k}_1 \cdot \vec{r})}$, $\varepsilon_2 e^{(-i\omega_2 t + i\vec{k}_2 \cdot \vec{r})}$ and $\varepsilon_3 e^{(-i\omega_3 t + i\vec{k}_3 \cdot \vec{r})}$ sequentially. Although the individual time ordered physical processes for R2 and R3 are different (i.e. absorption and emission) the phase matching and wave mixing are the same. This is summarized for all eight pathways in table 1.

Table 1: Paths, wave-vectors and envelope mixing for resonant TD4WM.

PATHWAY	PHASE MATCHING	WAVE-MIXING
R1, R4	$k_{\text{signal}} = k_1 - k_2 + k_3$	$\varepsilon_1 \varepsilon_2^* \varepsilon_3$
R2, R3	$k_{\text{signal}} = k_2 - k_1 + k_3$	$\varepsilon_1^* \varepsilon_2 \varepsilon_3$
R*1, R*4	$-k_{\text{signal}} = -k_1 + k_2 - k_3$	$\varepsilon_1^* \varepsilon_2 \varepsilon_3^*$
R*2, R*3	$-k_{\text{signal}} = k_1 - k_2 - k_3$	$\varepsilon_1 \varepsilon_2^* \varepsilon_3^*$

In the following analysis, we will only be concerned with the R1-R4 pathways. In the end, all paths must be considered in order to have a real output. In order to understand how the various pathways undergo the dynamic time evolution associated with the re-phasing condition of the SPE and the de-phasing condition associated with the VC, we next investigate the time evolution of the atomic response. This mathematical formulation will lead naturally to the pathways graphically depicted by the double-sided

Feynman diagrams of this section, as well as motivating the resulting macroscopic polarization responsible for the 4WM signal.

Green Function Perturbative Expansion

In a mathematical sense, Green functions are solutions to the partial differential equations of physics with a Dirac delta function as a driving term. Green function analysis is one of the most general and encompassing formulations of physics, insofar as its usefulness in describing a system evolving under a perturbative interaction. This is because a delta function impulse is a mathematically fundamental perturbation.

In quantum dynamics, operators either act to describe the functional evolution of a system (Schrodinger picture), or they evolve themselves, describing that aspect (the operator) of the system's evolution (Heisenberg picture). The time evolution operator of quantum dynamics,

$$U(t, t_0) = \exp\left[-\frac{i}{\hbar} H(t - t_0)\right] \quad (10)$$

when operating on a system, describes the propagation of that system:

$$|\alpha, t_0, t\rangle = U(t, t_0) |\alpha, t_0\rangle \quad (11)$$

In the Heisenberg picture the system is entirely described by the evolution of the time evolution operator, which obeys the Schrodinger equation.

$$i\hbar \frac{\partial U(t, t_0)}{\partial t} = H U(t, t_0) \quad (12)$$

Here H represents the Hamiltonian of the system $H = H_0 + H_1(t)$.

The time evolution operator may be decomposed as $U(t, t_0) = U_o(\tau)U_I(t_I)$. Where τ is the time period between interactions and t_I is the time of the interaction.

In time domain wave mixing, we want to find $U(t, t_0)$ for interaction potentials (H_I 's) applied at different times. To this end we rely on the solution known as the Dyson series¹⁷ which describes the systems behavior under time ordered interactions.

$$U(t, t_0) = 1 + \sum_{n=1}^{\infty} \left(\frac{i}{\hbar} \right)^n \int_0^{\infty} d\tau_{21} \int_0^{\infty} d\tau_{32} \dots \int_0^{\infty} d(t-t_n) U_o(t-t_n) H_I(t_n) \dots U_o(\tau_{32}) H_I(t_2) U_o(\tau_{21}) H_I(t_1) U_o(t_1, t_0) \quad (13)$$

Equation(13), applied to the initial state, describes the evolution of the system after n , non-commuting, time ordered perturbations.

$$|\alpha, t_0, t\rangle^{(n)} = U^{(n)}(t, t_0) |\alpha, t_0\rangle = 1 + \sum_{n=1}^{\infty} \left(\frac{i}{\hbar} \right)^n \int_0^{\infty} d\tau_{21} \int_0^{\infty} d\tau_{32} \dots \int_0^{\infty} d(t-t_n) U_o(t-t_n) H_I(t_n) \dots U_o(\tau_{32}) H_I(t_2) U_o(\tau_{21}) H_I(t_1) U_o(t_1 - t_0) |\alpha, t_0\rangle \quad (14)$$

The first term in the series expressed by equations (13) represents the zero order state. Next, the interaction potential is coupled to the zero order term; considered a first order perturbation. The next term describes, in full, a second order perturbation; coupling the first order perturbed term to another perturbative potential. The expansion goes on describing higher orders of perturbations.

The principle of composition states that a time translation may be broken up into 'smaller' consecutive translations as,

$$|\alpha, t_0, t_2\rangle = U(t_2, t_1) U(t_1, t_0) |\alpha, t_0\rangle. \quad (15)$$

so long as the time ordering is consecutive.

Due to the nature of quantum mechanical time and energy parameter relations, (i.e. uncertainty, Fourier relations), we expect the time evolution of such a system to be related to the energy evolution. To this extent the retarded QM Green function is introduced in terms of the quantum time evolution operator as,

$$G(t-t_0) = \theta(t-t_0) U(t, t_0). \quad (16)$$

Here, $\theta(\tau)$ is the Heavyside step function ($\theta(\tau)=1$ for $\tau > 0$; $\theta(\tau)=0$ for $\tau < 0$). Note that the presence of the Heavyside step function in the Green function ensures that the response of the quantum system to a perturbative impulse is causal.

The corresponding green function equation is:

$$i\hbar \frac{\partial G(t-t_0)}{\partial t} - H_I G(t-t_0) = i\hbar \delta(t-t_0). \quad (17)$$

Equations (16) and (17) illuminate how a delta function in the interaction perturbation, represents a step function in the time evolution of the system.

The time-domain Green function transforms into a frequency domain entity through the Laplace-Fourier relations^{16, 17}:

$$G(t-t_0) = -\frac{1}{2\pi i} \int_{-\infty}^{\infty} dE \exp[-\frac{i}{\hbar} E(t-t_0)] G(E) \quad (18)$$

$$G(E) = -\frac{i}{\hbar} \int_{-\infty}^{\infty} dt G(t-t_0) \exp[\frac{i}{\hbar} E(t-t_0)] \quad (19)$$

where the frequency domain Green function takes the form:

$$G(E) = \frac{1}{E - H + i\varepsilon}. \quad (20)$$

In order to understand the role that the Green function propagator plays in the dynamics of the atomic response, we next consider the Schrodinger equation in Liouville space with damped-driven dipole interaction in a two level atomic system.

Evolution

The time dependent Schrodinger equation of motion (SE) governs the evolution of a quantum system interacting with potentials. The quantum system of interest is the two level atom interacting with a perturbative waveform coupled through the dipole potential.

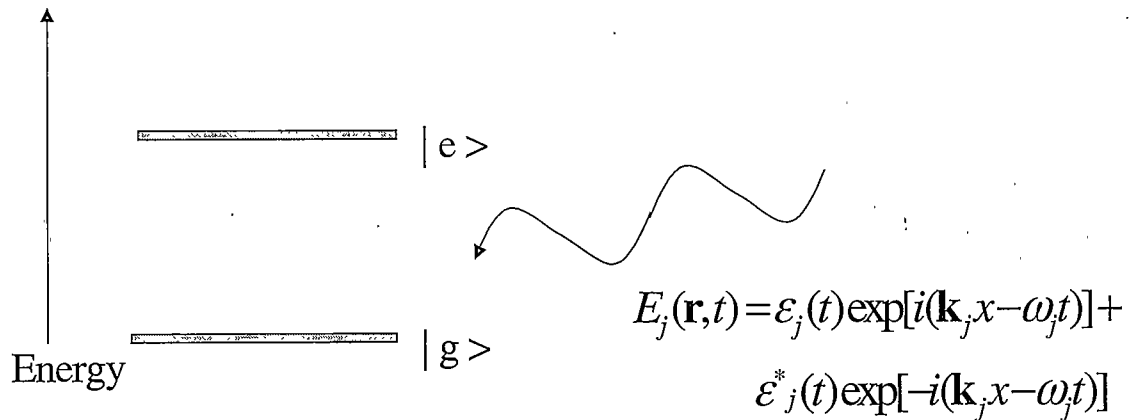


Figure 2.11: An optical waveform interacting with a two level atomic system.

The Liouville space Schrodinger equation describes the evolution of the atomic density operator

$$\frac{\partial \rho}{\partial t} = - \frac{i}{\hbar} \mathcal{L} \rho \quad (21)$$

Here, the Schrodinger equation is of the same form as when it acts on a quantum mechanical wave function, but is now governing the evolution of the density operator. This approach to the evolution of the density operator highlights the interchange between

coherence-states and populations. For an extensive treatment of the Schrodinger equation in Liouville space see reference [16].

The density operator is now in vector form,

$$|\rho(t)\rangle = \begin{bmatrix} \rho_{gg}(t) \\ \rho_{ee}(t) \\ \rho_{ge}(t) \\ \rho_{eg}(t) \end{bmatrix}. \quad (22)$$

The energy (atomic and interaction) is now described through the Liouville super-operator, \mathcal{L} , where each element of a 4 by 4 matrix is defined through its action on a Hermitian operator.

$$\mathcal{L} = \mathcal{L}_0 + \mathcal{L}_{\text{int}}(t) \quad (23)$$

$$\mathcal{L}_{\text{int}}(t) = E_j(t) \mathcal{V} \quad (24)$$

$$\mathcal{V}\rho = [V, \rho] \quad (25)$$

In equation (23), $\mathcal{L}_0\rho = [H_0, \rho]$, and the interaction super-operator, \mathcal{V} , couples the four density states (ρ_{gg} , ρ_{ee} , ρ_{eg} , ρ_{ge}) to each other (the electric field of equation (24) is real).

$$\mathcal{V} = \begin{bmatrix} \mathcal{V}_{gg,gg} & \mathcal{V}_{gg,ee} & -\mathcal{V}_{gg,eg} & \mathcal{V}_{gg,ge} \\ \mathcal{V}_{ee,gg} & \mathcal{V}_{ee,ee} & \mathcal{V}_{ee,eg} & -\mathcal{V}_{ee,ge} \\ -\mathcal{V}_{eg,gg} & \mathcal{V}_{eg,ee} & \mathcal{V}_{eg,eg} & \mathcal{V}_{eg,ge} \\ \mathcal{V}_{ge,gg} & -\mathcal{V}_{ge,ee} & \mathcal{V}_{ge,eg} & \mathcal{V}_{ge,ge} \end{bmatrix} \quad (26)$$

The matrix elements of equation (26) are operators defined by their action:

$$\mathcal{V}_{jk,mn}\rho_{mn} = V_{jm}\rho_{mn}\delta_{kn} - \rho_{mn}V_{kn}^*\delta_{jm} \quad (27)$$

Equation(27) is the Liouville expression for the commutation relations. This operation couples the initial state, ρ_{mn} , to the final state, ρ_{jk} . In equation (25), V is the dipole operator described as,

$$V(\mathbf{r}) = \sum_{\alpha} q_{\alpha}(\mathbf{r} - \mathbf{r}_{\alpha}). \quad (28)$$

The sum runs over electrons and nuclei(α), with charge q and position r . In equation (27)

$V_{ij} = \langle i|V|j\rangle$. Assuming no permanent dipole in the medium and no second order interaction,

$$\left. \begin{array}{l} \mathcal{V}_{ii,ii} = 0 \\ \mathcal{V}_{ij,ij} = 0 \end{array} \right\} \longleftarrow \text{No permanent dipole}$$

$$\left. \begin{array}{l} \mathcal{V}_{ij,ji} = 0 \\ \mathcal{V}_{ii,ji} = 0 \end{array} \right\} \longleftarrow \text{No second order coupling}$$

the interaction tetradic matrix applied to a ground initial state, ρ_{gg} , is:

$$\begin{bmatrix} 0 & 0 & -\mathcal{V}_{gg,eg} & \mathcal{V}_{gg,ge} \\ 0 & 0 & \mathcal{V}_{ee,eg} & -\mathcal{V}_{ee,ge} \\ -\mathcal{V}_{eg,gg} & \mathcal{V}_{eg,ee} & 0 & 0 \\ \mathcal{V}_{ge,gg} & -\mathcal{V}_{ge,ee} & 0 & 0 \end{bmatrix} \begin{bmatrix} \rho_{gg}(t) \\ 0 \\ 0 \\ 0 \end{bmatrix} = -\mathcal{V}_{eg,gg} \rho_{gg} + \mathcal{V}_{ge,gg} \rho_{gg} \quad (29)$$

$$= -V_{eg} \rho_{gg} + \rho_{gg} V_{ge}$$

The initial ground state may be perturbed into either of the coherence states, ρ_{ge} , or ρ_{eg} , as graphically described by the Feynman diagrams of Figure 2.7.

Thus far, phase evolution has not been addressed. The previous mentioned Green function propagator taking its Liouville-space form,

$$G(\tau) = \theta(\tau) e^{(-\frac{i}{\hbar} \mathcal{L}_0 \tau)}, \quad (30)$$

describes the dynamic time evolution. This operator is defined by its action on an initial state in Liouville space.

$$G_{ij}(\tau) \rho_i = e^{(-\frac{i}{\hbar} H_{oi} \tau)} \rho_i e^{(\frac{i}{\hbar} H_{oj} \tau)} \quad (31)$$

here, H_{oi} represents the energy eigenvalue of the i th state. The initial state coupled to the electric field through dipole interaction, is then propagated, yielding two evolution pathways. The first order perturbative expansion of the density operator is described with the aid of equations (13), (24) and (29) as:

$$\rho^{(1)}(t) = -\left(\frac{i}{\hbar}\right)^{(1)} \int_0^{\infty} d\tau [e^{(-\frac{i}{\hbar} H_e \tau)} \mathcal{V}_{eg,gg} \rho_{gg} e^{(\frac{i}{\hbar} H_g \tau)} + e^{(-\frac{i}{\hbar} H_g \tau)} \mathcal{V}_{ge,gg} \rho_{gg} e^{(\frac{i}{\hbar} H_e \tau)}] E(\mathbf{r}, t - \tau). \quad (32)$$

The paths,

$$G_{eg}(\tau) \mathcal{V}_{eg,gg} \rho_{gg} = e^{(-\frac{i}{\hbar} H_e \tau)} \mathcal{V}_{eg,gg} \rho_{gg} e^{(\frac{i}{\hbar} H_g \tau)}, \quad (33)$$

$$G_{ge}(\tau) \mathcal{V}_{ge,gg} \rho_{gg} = e^{(-\frac{i}{\hbar} H_g \tau)} \mathcal{V}_{ge,gg} \rho_{gg} e^{(\frac{i}{\hbar} H_e \tau)}$$

of equation (29), describe the evolution of the system until another perturbation occurs after a period, τ . The initial states first order perturbative evolution, described by equation (33), may then be perturbed again and undergo subsequent evolution. This is precisely described by the Dyson series of equation (13). However, due to the nature of coupling in Liouville space, the integral expressed in equation (14) contains multiple pathways. The system, in going from the pure initial state to the final coherence-state, is allowed various pathways specifically because the system is Hermitian.

The motivation behind applying equation (33) into equation (14) is expressed through the Feynman calculus and is beyond the scope of this thesis. However, for a lighter treatise on the relation between the green function evolution operator and the allowed paths, ultimately connected to the composition relation of equation (16), (see reference [17, 18]).

Each of the dynamic evolutions described by equation (33) is considered a Liouville-space generating function (LGF). The LGF's constitute the atomic portion of the overall semi-classical description. This is due to the electric field not appearing in equation (24). When the field is included, the expectation value of the dipole operator is the macroscopic polarization. When the field is not included, we are left with the atomic response function (see equation (47)), which, in principle, contains all of the microscopic information of the system¹⁶. The present formulation is continued through the entire 4WM input sequence. The field is then considered in order to determine the TD4WM signal.

We follow this line of reasoning through three orders of perturbation in all, yielding eight pathways directly related to the eight Feynman diagrams of Figure 2.9 and Figure 2.10. For sake of brevity, we will only shown the pathways R1-R4. In the end the conjugate paths, R*1-R*4 must also be accounted for in order to have a real signal.

$$\begin{aligned}
 \rho_1(\tau_{21}) &= e^{\left(\frac{-i}{\hbar}H_e\tau_{21}\right)} V_{eg} \rho_{gg} e^{\left(\frac{i}{\hbar}H_g\tau_{21}\right)} \\
 \rho_1(\tau_{21} + \tau_{32}) &= e^{\left(\frac{-i}{\hbar}H_e\tau_{32}\right)} \rho_1(\tau_{21}) V_{ge} e^{\left(\frac{i}{\hbar}H_g\tau_{32}\right)} \\
 \rho_1(\tau_{21} + \tau_{32} + (t-t_3)) &= e^{\left(\frac{-i}{\hbar}H_e(t-t_3)\right)} \rho_1(\tau_{21} + \tau_{32}) V_{eg} e^{\left(\frac{i}{\hbar}H_g(t-t_3)\right)}
 \end{aligned} \tag{34}$$

$$\begin{aligned}
\rho_2(\tau_{21}) &= e^{\left(\frac{-i}{\hbar}H_g\tau_{21}\right)} \rho_{gg} V_{ge} e^{\left(\frac{i}{\hbar}H_e\tau_{21}\right)} \\
\rho_2(\tau_{21} + \tau_{32}) &= e^{\left(\frac{-i}{\hbar}H_g\tau_{32}\right)} V_{eg} \rho_2(\tau_{21}) e^{\left(\frac{i}{\hbar}H_e\tau_{32}\right)} \\
\rho_2(\tau_{21} + \tau_{32} + (t-t_3)) &= e^{\left(\frac{-i}{\hbar}H_e(t-t_3)\right)} \rho_2(\tau_{21} + \tau_{32}) V_{eg} e^{\left(\frac{i}{\hbar}H_g(t-t_3)\right)}
\end{aligned} \tag{35}$$

$$\begin{aligned}
\rho_3(\tau_{21}) &= e^{\left(\frac{-i}{\hbar}H_g\tau_{21}\right)} \rho_{gg} V_{ge} e^{\left(\frac{i}{\hbar}H_e\tau_{21}\right)} \\
\rho_3(\tau_{21} + \tau_{32}) &= e^{\left(\frac{-i}{\hbar}H_g\tau_{32}\right)} \rho_3(\tau_{21}) V_{eg} e^{\left(\frac{i}{\hbar}H_e\tau_{32}\right)} \\
\rho_3(\tau_{21} + \tau_{32} + (t-t_3)) &= e^{\left(\frac{-i}{\hbar}H_e(t-t_3)\right)} V_{eg} \rho_3(\tau_{21} + \tau_{32}) e^{\left(\frac{i}{\hbar}H_g(t-t_3)\right)}
\end{aligned} \tag{36}$$

$$\begin{aligned}
\rho_4(\tau_{21}) &= e^{\left(\frac{-i}{\hbar}H_e\tau_{21}\right)} V_{eg} \rho_{gg} e^{\left(\frac{i}{\hbar}H_g\tau_{21}\right)} \\
\rho_4(\tau_{21} + \tau_{32}) &= e^{\left(\frac{-i}{\hbar}H_g\tau_{32}\right)} V_{ge} \rho_4(\tau_{21}) e^{\left(\frac{i}{\hbar}H_e\tau_{32}\right)} \\
\rho_4(\tau_{21} + \tau_{32} + (t-t_3)) &= e^{\left(\frac{-i}{\hbar}H_e(t-t_3)\right)} V_{eg} \rho_4(\tau_{21} + \tau_{32}) e^{\left(\frac{i}{\hbar}H_g(t-t_3)\right)}
\end{aligned} \tag{37}$$

Equations (34)-(37) describe the interaction and evolution of the system for the four Liouville pathways, R1-R4. Here, $\rho_\alpha(\tau_{21} + \tau_{32} + (t-t_3))$ with $\alpha=1-4$, are the time-domain 4WM Liouville Generating Functions. This representation is a path integral¹⁶.

Equation (32) expressed for TD4WM is:

$$\begin{aligned}
\rho^{(3)}(t) &= -\left(\frac{i}{\hbar}\right)^{(3)} \int_0^\infty d(t-t_3) \int_0^\infty d\tau_{32} \int_0^\infty d\tau_{21} \overline{\rho}^{(3)}(\tau_{21} + \tau_{32} + (t-t_3)) \\
&\quad E(\mathbf{r}, t-t_3) E(\mathbf{r}, t-t_3-\tau_{32}) E(\mathbf{r}, t-t_3-\tau_{32}-\tau_{21})
\end{aligned} \tag{38}$$

where

$$\begin{aligned} \overline{\rho}^{(3)}(\tau_{21} + \tau_{32} + (t - t_3)) = & \sum_{\alpha=1}^4 |e\rangle \rho_{\alpha}(\tau_{21} + \tau_{32} + (t - t_3)) \langle g| \\ & - \sum_{\alpha=1}^4 |g\rangle \rho_{\alpha}^{\dagger}(\tau_{21} + \tau_{32} + (t - t_3)) \langle e| \end{aligned} \quad (39)$$

This representation describes the interchange of population and coherence evolution periods. A key feature of the evolution described in equations (34)-(37) is the nature of the phase dynamics in the periods τ_{21} and $t - t_3$ of $\rho_{\alpha}(\tau_{21} + \tau_{32} + (t - t_3))$. For $\alpha = 2, 3$, the evolution described by the Green function propagators during the two periods are phase conjugate. One set has rephasing behavior of the coherence state, which eliminates the effects of inhomogeneous dephasing when $t - t_3 = \tau_{21}$. For $\alpha = 1, 4$ the phase evolution is not conjugate during the two time periods so that the phase established in the first period, simply continues to evolve in a de-phasing manner during t_3 . This then describes the conjugate nature of the pathways depicted with the TD4WM Feynman diagrams.

The general character of the inhomogeneous phase evolution of all paths for the three time periods is depicted in Figure 2.12. There are four, instead of eight, paths needed to describe the inhomogeneous phase evolution of the system. This is because the inhomogeneous phase evolution leads to a real electric field output and therefore conjugate terms of equation (39) experience the same inhomogeneous phase behavior.

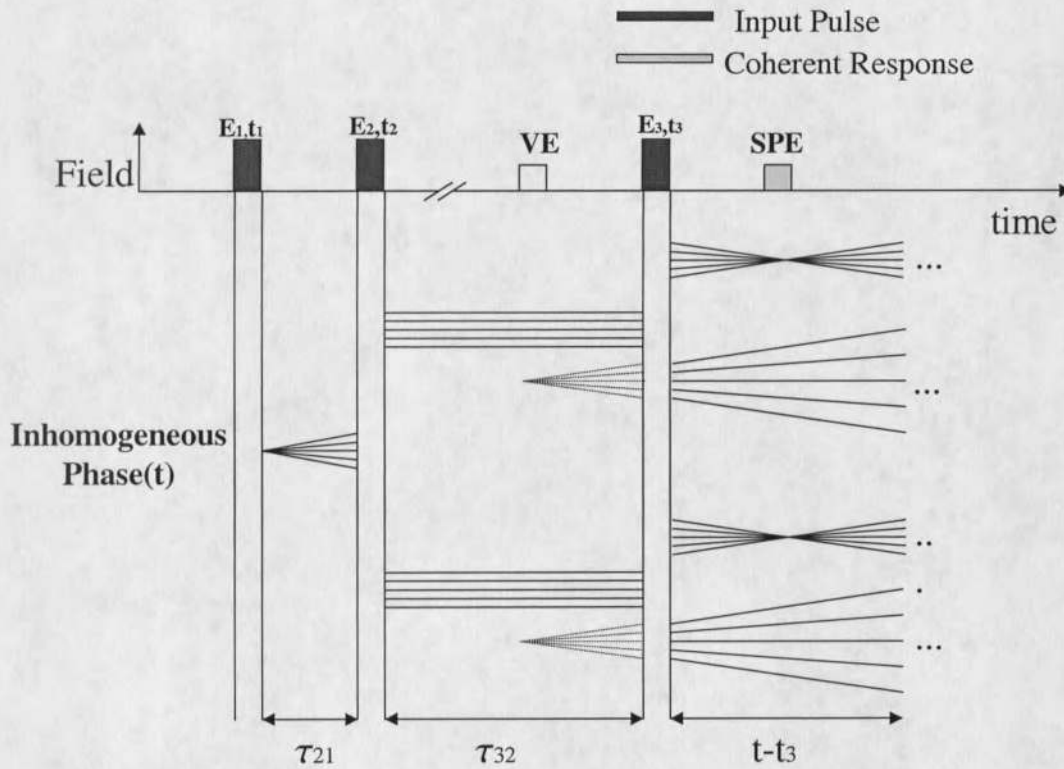


Figure 2.12: Time-domain 4WM input sequence with corresponding coherence-state phase evolution.

Figure 2.12 describes the inhomogeneous phase evolution of the system for TD4WM. The third pulse stimulates conjugate phase evolution paths from the excited and ground state gratings which are represented by sets of parallel lines in Figure 2.12. One path stimulated from each grating is undergoing inhomogeneous rephasing, while another continues to undergo inhomogeneous dephasing. At τ_{21} after pulse 3 the oscillating dipoles are rephased and the stimulated photon echo is emitted.

Next, we relate the atomic response function and the macroscopic polarization, ultimately responsible for the echo signal.

The Atomic Response in Time Domain Four-Wave Mixing

The macroscopic polarization, $P(\mathbf{r}, t)$, is the medium's source term for the Maxwell equation. We are therefore most interested in how to describe the polarization in terms of an atomic response to input waveforms. The semi-classical equations of interest are the Maxwell-Liouville equations¹⁶, given as:

$$\nabla \times \nabla \times E(\mathbf{r}, t) + \frac{1}{c^2} \frac{\partial^2}{\partial t^2} E(\mathbf{r}, t) = -\frac{4\pi}{c^2} \frac{\partial^2}{\partial t^2} P(\mathbf{r}, t), \quad (40)$$

$$P(\mathbf{r}, t) = \text{Tr}[V \rho(t)], \quad (41)$$

$$\frac{\partial \rho}{\partial t} = -\frac{i}{\hbar} \mathcal{L} \rho. \quad (42)$$

A perturbative expansion, of the space and time dependant polarization $P(\mathbf{r}, t)$, to the n th power in the radiation field, where input waveforms act to first order, is given by the expectation value of the dipole operator with the density operator being expanded to the n th order in the field.

$$P^{(n)}(\mathbf{r}, t) = \text{Tr}[V \rho^{(n)}(t)] \quad (43)$$

In order to find the polarization to third order in the field, it is only necessary to find the density operator expressed to third order. As stated earlier, the perturbative expansion of the density operator is semi-classical. The atomic nature of the density operators' evolution is given by the LGF's of the previous section. In analogy to equation (46), we can define the third order atomic response function, $R_\alpha((t-t_3), \tau_{21}, \tau_{32})$, as the expectation of the dipole transition (ignoring the field).

$$R_\alpha((t-t_3), \tau_{21}, \tau_{32}) = \text{Tr}[V_{g\alpha}, \rho_\alpha(\tau_{21} + \tau_{32} + (t-t_3))] \quad (44)$$

Here, $\alpha=1, \dots, 4$ and $\rho_\alpha(\tau_{21} + \tau_{32} + (t-t_3))$ are the LGF's of equations (34)-(37).

It is now convenient to separate this response function into homogeneous and inhomogeneous contributions as follows:

$$R_\alpha((t-t_3), \tau_{21}, \tau_{32}) = R^H_\alpha((t-t_3), \tau_{21}, \tau_{32}) \chi((t-t_3) \pm \tau_{21}) \quad (45)$$

Here, $R^H_\alpha(t_3, \tau_{21}, \tau_{32})$ is the homogeneous contribution to the nonlinear response representing the dynamic contributions to the response function in the absence of inhomogeneous broadening. The inhomogeneous portion, $\chi(t_3 \pm \tau_{21})$, represents the static contribution and is the inverse Fourier transform of the inhomogeneous frequency distribution, $g(\omega)$.

$$g(\omega) = \frac{1}{2\pi} \int_0^+ dt \chi(t) e^{i\omega t} \quad (0.46)$$

$\chi(t)$ represents the inhomogeneous dephasing or rephasing behavior of the system. This function not only peaks or decays with the TD4WM signal but also contains the pertinent frequency information of the spectral grating.

The third order nonlinear polarization, responsible for the TD4WM signal, may be expressed in terms of the nonlinear response functions, $R_\alpha((t-t_3), \tau_{21}, \tau_{32})$, as:

$$P^{(3)}(\mathbf{k}_{a,b}, t) = \left(\frac{i}{\hbar}\right)^3 \int_0^\infty d(t-t_3) \int_0^\infty d\tau_{32} \int_0^\infty d\tau_{21} \\ \left[[R^H_2((t-t_3), \tau_{32}, \tau_{21}) + R^H_3((t-t_3), \tau_{32}, \tau_{21})] \chi((t-t_3) - \tau_{21}) E_1^* E_2 E_3 e^{i\Delta(t-t_2)} \right]_a + \quad (47) \\ \left[R^H_1((t-t_3), \tau_{32}, \tau_{21}) + R^H_4((t-t_3), \tau_{32}, \tau_{21}) \right] \chi((t-t_3) + \tau_{21}) E_1 E_2^* E_3 e^{i\Delta(t+t_2)} \right]_b]$$

with the spatial phase matching conditions given by (see table 1):

$$\mathbf{k}_a = \mathbf{k}_3 + \mathbf{k}_2 - \mathbf{k}_1 \quad (48)$$

$$\mathbf{k}_b = \mathbf{k}_3 - \mathbf{k}_2 + \mathbf{k}_1 \quad (49)$$

The elimination of the inhomogeneous dephasing process by the rephasing of each member of the inhomogeneous ensemble is the key to the SPE event, which reaches its maximum intensity at $\chi(t_3 - \tau_{21} = 0)$. For the given conditions, only the first term of equation (47) will contribute to the echo signal. In order for $\chi(t_3 + \tau_{21} = 0)$, t_3 would have to have a value of $-\tau_{21}$. This violates the causal principle, however because of the causal form of the green function propagators, there is no mathematical inconsistency. The second term of equation (49) does not contribute to the SPE signal because the inhomogeneous contribution is negligible, as given by $\chi(t_3 + \tau_{21} = 0)$. The connection to the phase evolution is specifically described in the propagation period t_3 of equations (34) -(37), where rephasing occurs under the condition $[G_{eg}((t - t_3) = \tau_{21})] = G_{ge}(\tau_{21})$ of equations (35) and (36).

The double-sided Feynman diagrams, for optical coherent transient TD4WM in a two level system that contribute to the SPE event are given in Figure 2.11, including the corresponding propagators.

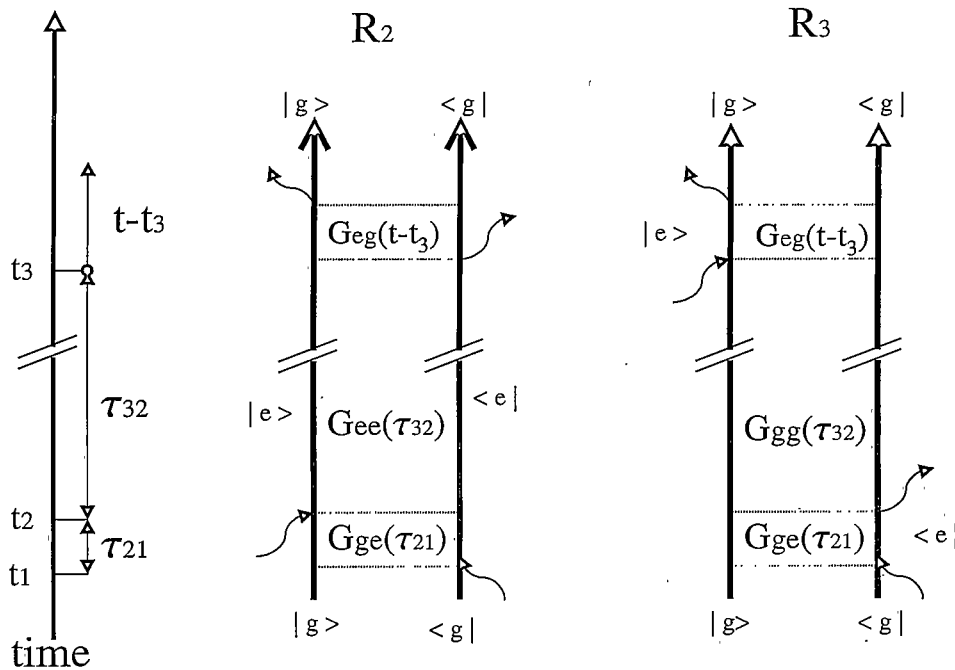


Figure 2.13: The double-sided Feynman diagrams of time-domain four wave-mixing (SPE contribution).

Thus we have shown that only the first term of equation (47) contributes to the SPE event. The experimental undertaking of this study is to interact with the second term of equation(47) (response function pathways R1, R4), which does not participate in the SPE event, and experimentally verify their relationship to the R2, R3 pathways.

Correspondence

We are now in a position to qualitatively address the correspondence of the holographic events by letting τ_{21} increase from zero. This corresponds to transforming a spatial holographic grating to a frequency domain grating. In the case of a spatially modulated grating, part of the recall pulse scatters symmetrically to both sides. As the

delay is increased, only a single holographic event (SPE) is emitted from the three beam input scheme as described in this chapter. This loss of scattering symmetry is due to the spatial grating being replaced by a spatial-spectral grating as τ_{21} is increased from zero¹⁵. This can be understood through the Kramers-Kronig dispersion relations which relate a frequency grating to an index of refraction grating that in turn implies a time delay of the scattered waveform. And due to an upper limit on the speed of light, scattering can not occur in the time forward direction. In the TD4WM theory presently developed, it appears that the holographic symmetry of a phase conjugate response pair, found in the first order scattered electric fields of spatial holography, is retained in the coherence-state pathways of spatial-spectral holography. The impelling evidence is that both the spatial grating and the spectral grating response satisfy identical spatial phase matching conditions, and both have a phase-conjugation-symmetry associated with the holographic process.

The experimental work in this thesis quantitatively relates the phase conjugate set of coherence-state pathways represented by R1, R4 and R2, R3. This is accomplished through a six-wave mixing input scheme that rephases both of the conjugate paths to emit echo signals. These signals are then characterized.

CHAPTER 3

EXPERIMENTAL TECHNIQUES

Introduction

Energy source studies of the SPE¹⁹ indicate that the 4WM coherence-state energy is reduced on the order of ~10% after the echo event. Therefore a portion of the ions involved in the 4WM coherence-state are unaltered by the SPE event and continue their phase evolution. Then, all coherence-state pathways are undergoing inhomogeneous dephasing (see Figure 2.12). If a π -pulse is input into the system after the SPE, then the phase evolution of the coherence-state would be inverted causing all coherence-state pathways to undergo inhomogeneous rephasing. The result of this scenario would be the emission of time-ordered echo events associated with the conjugate 4WM coherence-state paths (depicted in Figure 3.1). This technique constitutes a six-wave mixing (6WM) process, and has the advantage of exploiting the fully rephased character of all paths. Through this technique, the experimental studies presented in this thesis qualitatively measure the relation between coherence-state pathways associated with the SPE and VE.

Six Wave-Mixing

If the π -pulse (pulse 4) is introduced after the SPE, then all four response function pathways (R1-R4) rephase to emit echoes, called here the rephased SPE (R-SPE) and rephased VE (R-VE).

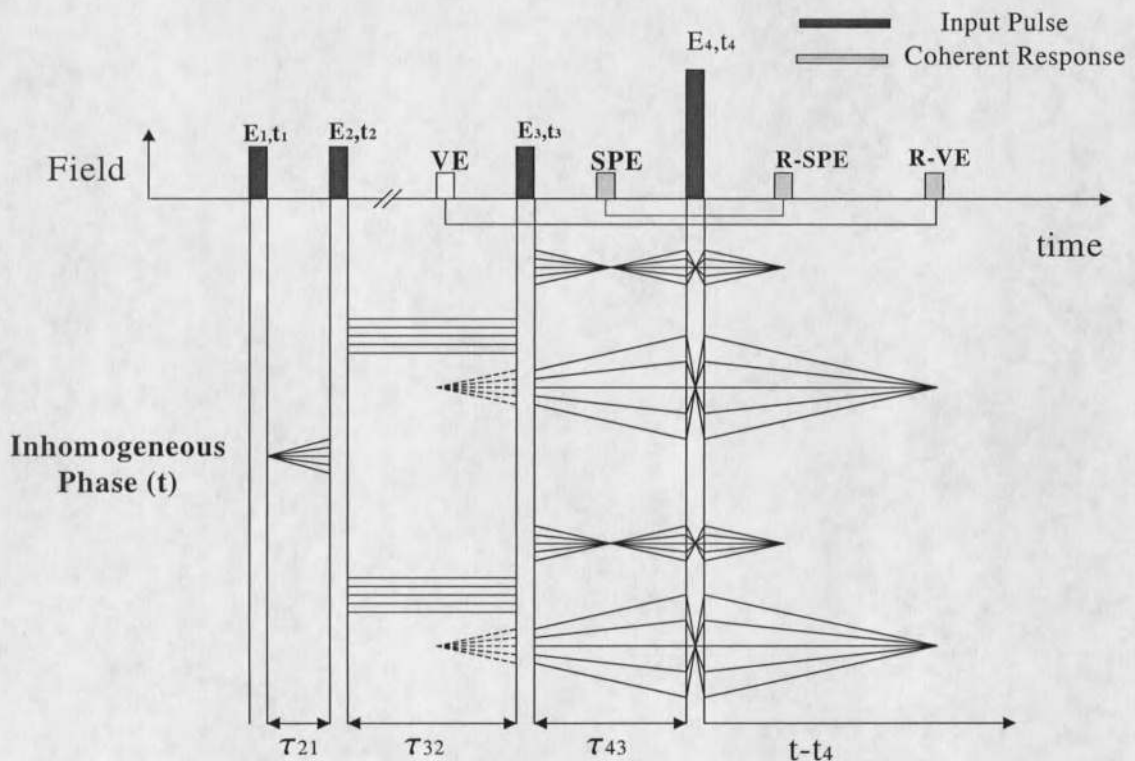


Figure 3.1: The six wave-mixing technique used to rephase all four wave-mixing coherence-state paths.

It is interesting to note that the R-SPE may be viewed as a second order echo. This is to say, in a two-pulse photon echo experiment¹⁵, pulse 1 creates a coherence-state, which at a later time undergoes inhomogeneous rephasing due to a π -pulse,

resulting in a two pulse photon echo (PE). In contrast, the SPE is a pulse that was created by a coherence-state. However, at the time of the SPE, whether the coherence created the pulse or the pulse created the coherence, the subsequent evolution of that coherence-state pathway is identical. The R-SPE can then be thought of as a two-pulse photon echo of the SPE-E₄ sequence. The π -pulse inverts the phase evolution of all coherence-state paths. If the SPE pathways were the only existing coherence-state terms during the evolution period τ_{32} , then the VC would not rephase to emit a signal. However, due to the nature of the pathologies of the 4WM sequence, the R1, R4 coherence-state pathways also undergo rephasing, resulting in the emission of the R-VE.

Experiments

The R-SPE and R-VE are characterized as follows: Experiment I verifies that the signals are products of the 6WM process by fixing the pulse input timing and decreasing the area of pulse 4 (θ_4). This has the effect of increasing any 4WM signal and decreasing any 6WM signal that pulse 4 is involved in. Experiment II measures the dynamic coherence loss (loss of relative phase of the coherence-state) as a function of echo signal attenuation, by varying τ_{21} . Coherence loss is a measure of the lifetime of a coherence-state and therefore relates the 6WM signals to a common coherence-state origin. Lastly, Experiment III verifies the phase conjugate nature of the 6WM signals. When a temporally complex waveform is introduced for pulse 2 and 3, the 4WM signal (SPE) represents a time-domain auto-convolution of the complex waveform, whereas the VE represents a time-domain auto-correlation. The distinction between time-domain

correlation and convolution is a temporal inversion²⁰ in the signal processing. This expresses the phase-conjugate nature of the two pathways.

Experimental Set-Up

The experimental set-up used in all the experiments presented in this thesis is depicted in Figure 3.2.

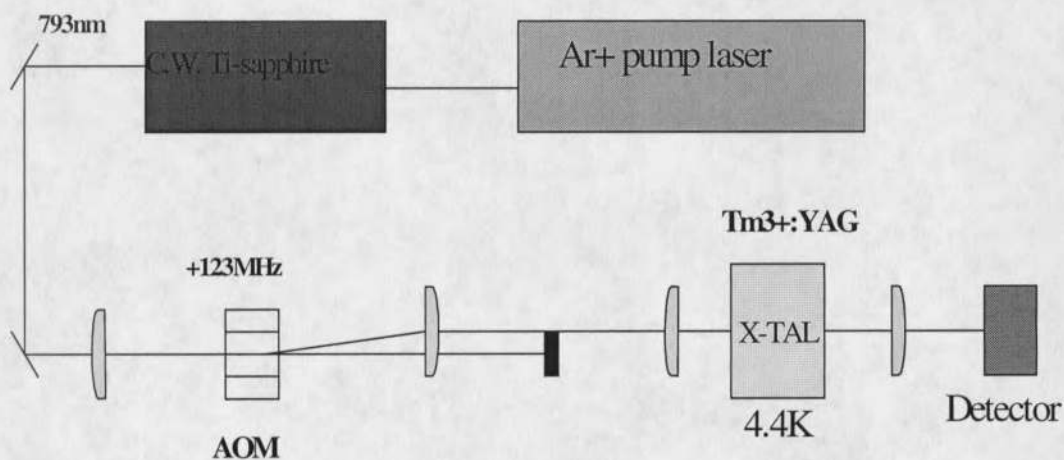


Figure 3.2: Six wave-mixing experimental apparatus.

All experiments are done in a 7mm long Tm^{3+} :YAG crystal (.1 at. %), held at 4.4K with a continuous flow liquid helium cold-finger cryostat. The laser system consists of an argon-ion (16.4 W) pumped Ti: sapphire ring-laser (1.5 W), single-mode frequency locked at 793nm, resonant with the ${}^3H_6 \rightarrow {}^3H_4$ transition of the thulium ion. The linear

polarized beam was crafted into pulsed waveforms by an acousto-optic modulator driven by a 1.0 GHz arbitrary waveform generator, then focused in a 200 μm spot ($1/e^2$ diameter) in the crystal along a direction parallel to a single dipole orientation. All experiments were performed on a single beam due to the time-ordered nature of the 4WM and 6WM signals. Temporal gating of the pulse sequence was accomplished with delay electronics. The signals were detected with a FND 100 photo-diode and captured on a TEK digital oscilloscope averaging 256 times.

An optimized (π -pulse) was found through the optical nutation technique of Sun²¹. Keeping the bandwidth constant, the power of the π -pulse was quartered to produce the $\pi/2$ -pulse waveforms.

Material Considerations

As stated earlier, the SPE is a product of time ordered resonant pulses interacting with a medium that is inhomogeneously broadened in its electronic absorption spectrum. The coupling to the thermal bath is the dominant inhibitor of the rephasing process and constrains the echo experiment to an ultra-cold environment achieved through a table-top cryogenic system. Scientific Material Corp. prepared the single dipole Tm^{3+} : YAG sample. The parameters for the 7mm long Tm^{3+} : YAG (at .1%) crystal are given in table 2, where Γ_1 is the inhomogeneous linewidth, T_2 is the dephasing relaxation parameter, T_1 is the upper-state lifetime and α is the absorption coefficient.

The experimentally measured dephasing relaxation time (T_2) was found by assuming exponential signal decay and measuring the SPE from a traditional input

sequence while changing τ_{21} and looking for the signal intensity to drop by $1/e$, that being a general indicator of T_2 (see equation (50)).

The absorption length (αL) was found by introducing a weak waveform into the material and measuring the change in absorption of the pulse as it was tuned off resonance.

Table 2: Tm^{3+} : YAG (at. .1%) 7.0-mm parameters:

PARAMATER	VALUE
Γ_1	17GHz
T_2	23.4 μs
T_1	800 μs
α	1.5cm ⁻¹

Experiment I: 4WM and 6WM Signal Dependence on θ_4

In practice, the 6WM input scheme of Figure 3.1 will produce other signals due to 4WM processes with which pulse 4 is involved. Pulse 4 may act like a $\pi/2$ -pulse and scatter off the spatial-spectral grating to produce a SPE from the E_1, E_2, E_4 sequence. As well, pulse 3 and pulse 4 together can produce a two pulse photon echo. These, along with the R-SPE and R-VE are the dominant signals of the total 6WM input sequence, depicted in Figure 3.3.

Each of the echo signals occurring in the time-domain $t > t_4$ may be verified by reducing the area of pulse 4 (θ_4)(initially optimized as a π -pulse). The corresponding increase (decrease) in signal intensity corresponds to θ_4 acting as a π -pulse ($\pi/2$ -pulse). The area of pulse 4 is reduced, by decreasing the electric field amplitude through the arbitrary waveform generator.

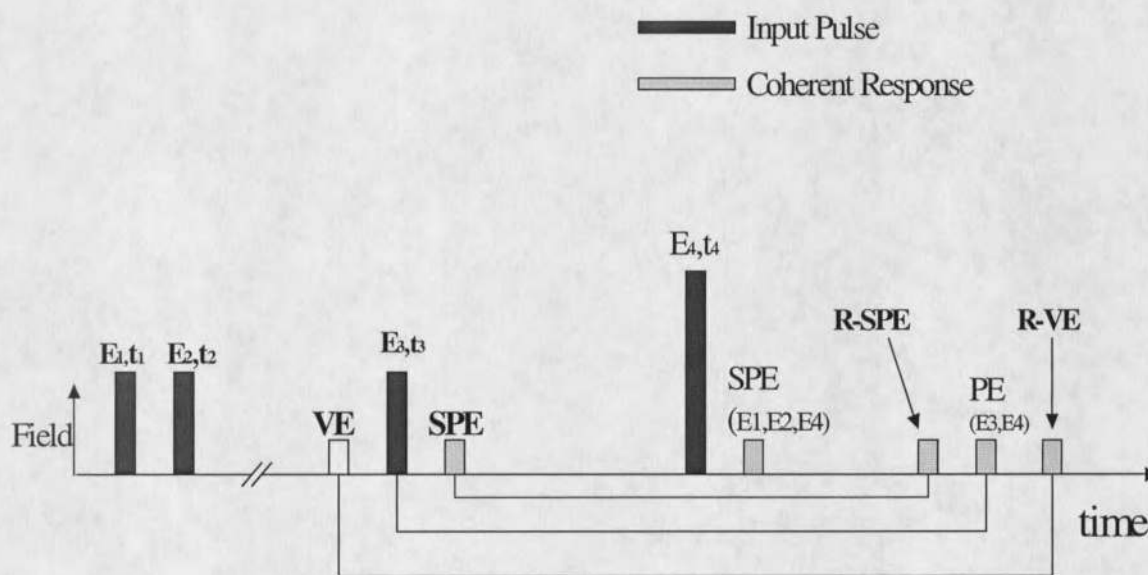


Figure 3.3: The expected four and six wave-mixing signals generated from the 6WM input scheme.

The expected signal outputs for the 6WM technique are given in Figure 3.3. The four entities shown rely on the area of pulse 4 in different ways. The R-SPE, R-VE, and $2PE_{3,4}$ are optimized for pulse 4 to have an area, $\theta_4 = \pi$. The $SPE_{(E1, E2, E4)}$ is optimized if $\theta_4 = \pi/2$.

The captured signals for 6WM with variable θ_4 are given in Figure 3.4, Figure 3.5 and Figure 3.6. Figure 3.4 shows the captured pulse sequence, beginning at t_3 . Figure

3.4 shows the dependence of the latter three signals on θ_4 , R-SPE, PE (E_3 , E_4) and R-VE, time ordered respectively.

In Figures 3.5 and 3.6, θ_4 is initially optimized as a π -pulse, given by the (\square) trace. The area is subsequently reduced in two steps, given by the (Δ) and (\square) traces respectively. The reduction in signal intensity with decreasing θ_4 , for the three echoes, demonstrates their dependence on pulses 4 acting to second order in the field. Figure 3.6 shows SPE (E_1 , E_2 , E_4) for the same capture sequence. The signal increases with reduction in θ_4 , demonstrating its dependence on pulse 4 acting to first order in the field.

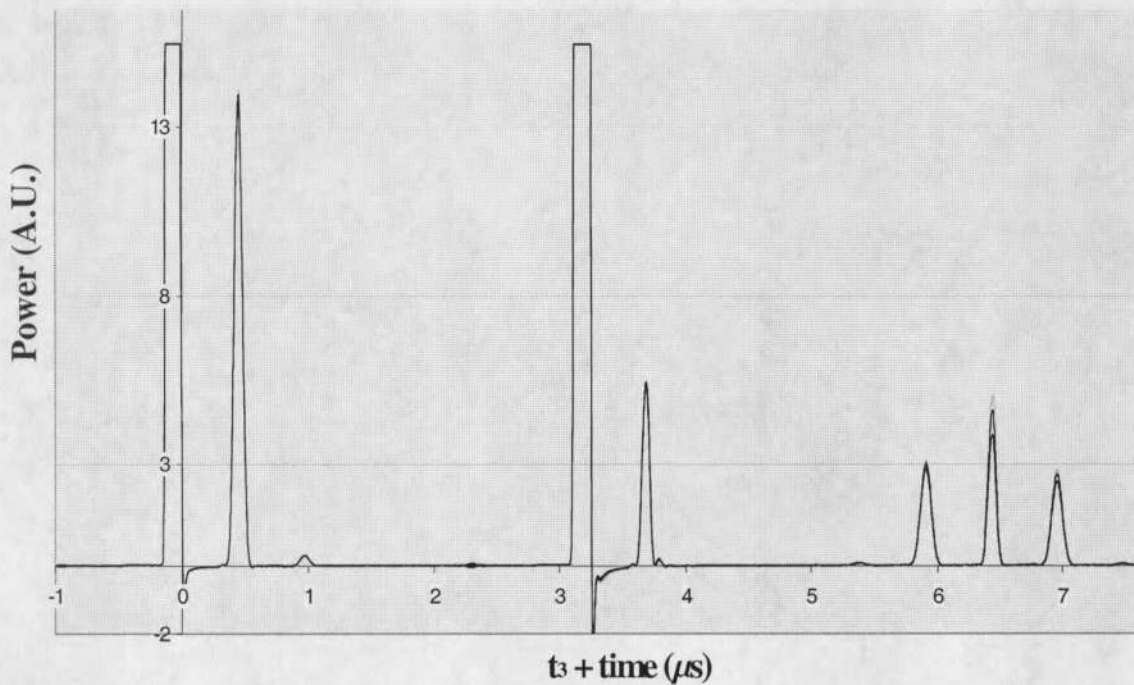


Figure 3.4: Six wave-mixing with variable θ_4 .

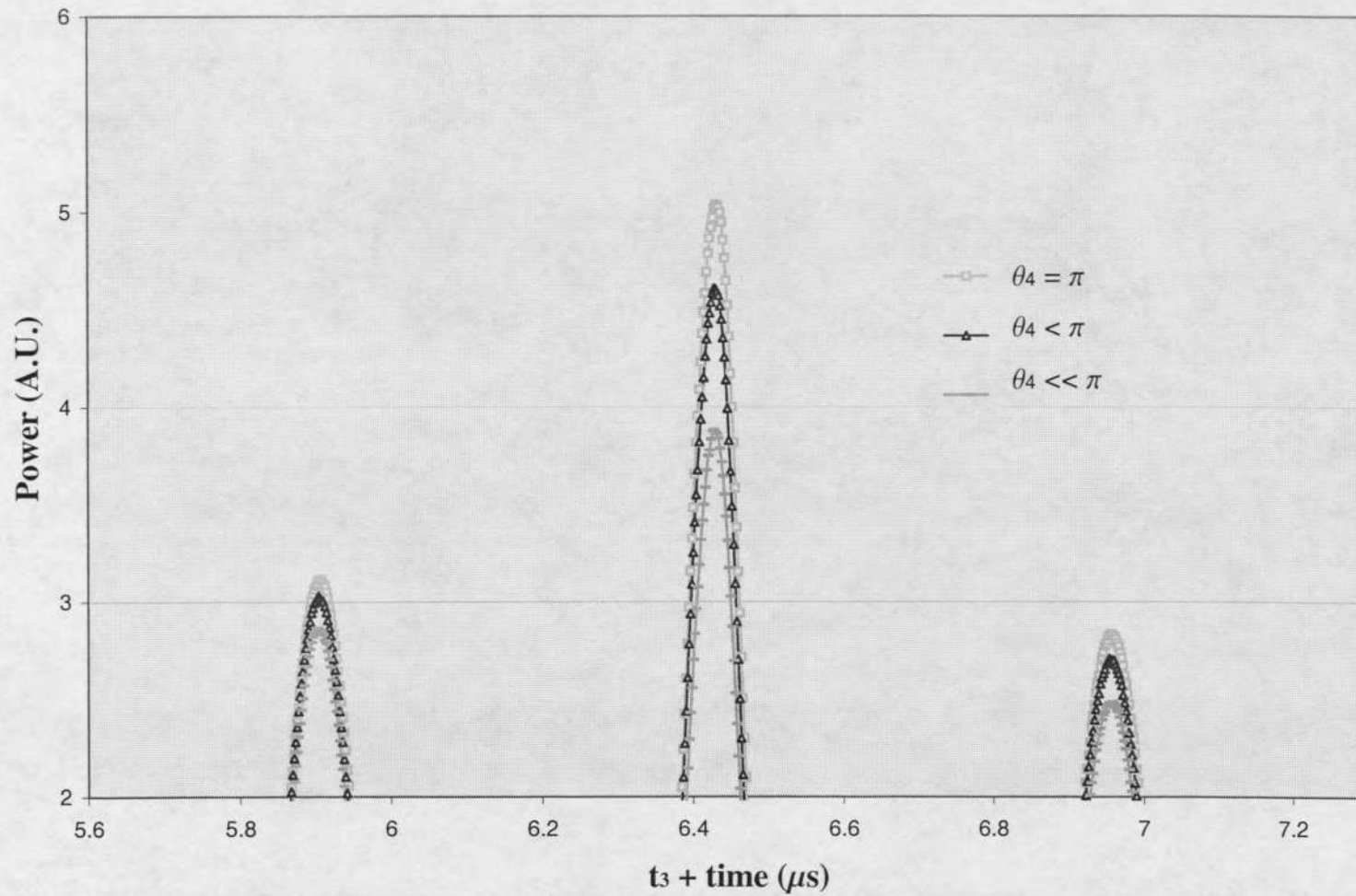


Figure 3.5: Six wave-mixing with variable θ_4 . Signal attenuation of R-SPE, PE(E_3, E_4) and R-VE with variable θ_4 .

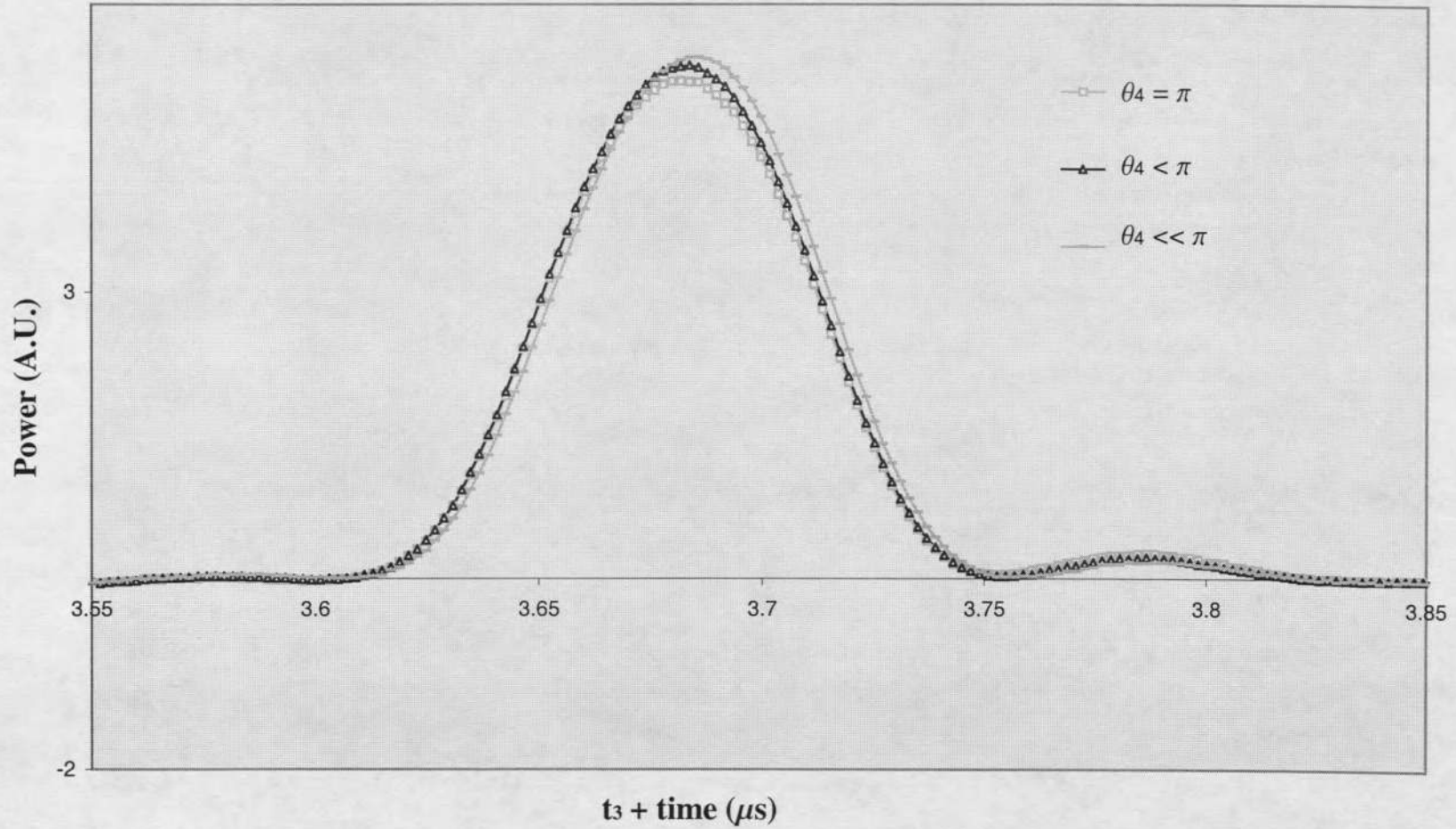


Figure 3.6: Six wave-mixing with variable θ_4 . Signal increase of SPE (E_1, E_2, E_4) with variable θ_4 .

Experiment II: 6WM with Variable τ_{21}

Coherence loss is a non-reversible loss of phase relation between the frequency components of the coherence-state, as described in the 'material considerations' section. It is phenomenologically modeled as exponential signal attenuation (equation (50)) dependent upon the coherence time, t_{coh} (the time that the system spends in a coherence-state).

$$I = I_0 e^{\frac{-2t_{\text{coh}}}{T_2}} \quad (50)$$

The expected coherence time of the R-SPE and R-VE is given as:

$$\begin{aligned} t_{\text{coh(R-SPE)}} &= 2t_4 - 2t_3 \\ t_{\text{coh(R-VE)}} &= 2t_4 - 2t_3 - 2\tau_{21} \end{aligned} \quad (51)$$

Although the R-SPE and R-VE are temporally unique, as τ_{21} approaches zero the two signals should converge on a common intensity and temporal location, as given by equation (50) and (51). The coherence time of the R-SPE is independent of τ_{21} , while the R-VE is dependant upon $2\tau_{21}$. This implies that a variation in τ_{21} will not effect the R-SPE intensity, only its temporal location. Conversely, the R-VE will attenuate according to equation (50).

Six wave-mixing with brief (80ns) pulses is experimentally demonstrated with the delay, τ_{21} , being varied from .32 μs to 2.24 μs in .32 μs intervals. The captured waveforms are shown in Figure 3.7 and the intensities of the R-SPE (\square 's) and R-VE (Δ 's) versus τ_{21} is plotted in Figure 3.8, along with theoretical curves.

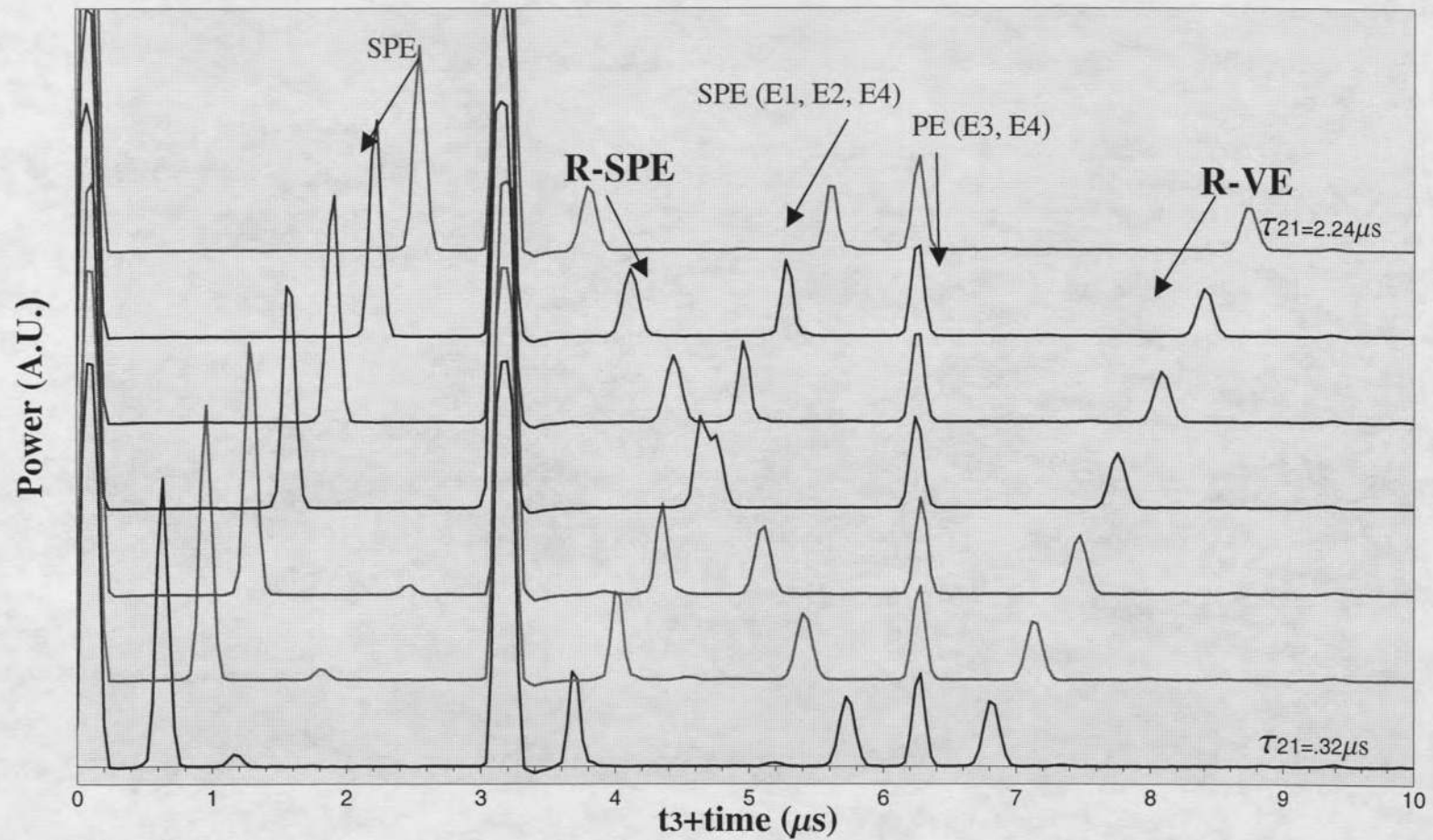


Figure 3.7: Captured signals for 6Wm with variable τ_{21} . The delay ranges from $.32 \mu\text{s}$ to $2.24 \mu\text{s}$ in $.32 \mu\text{s}$ steps .

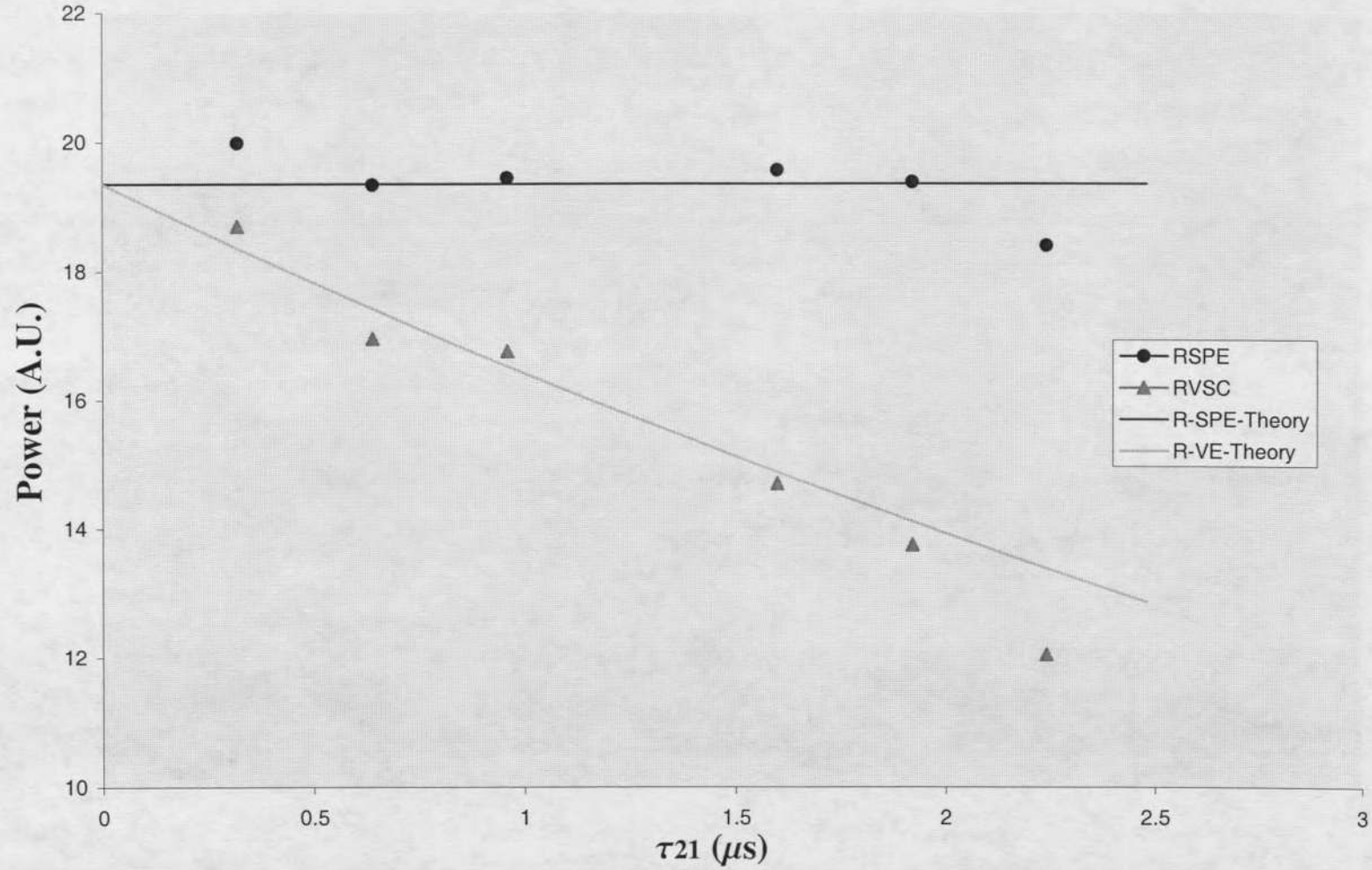


Figure 3.8: Power of R-SPE and R-VE vs. τ_{21} along with theoretical fits.

The upper theoretical curve in Figure 3.8 represents the average of the detected R-SPE signals. The lower curve is then fit to the $\tau_{21}=0$ point of the upper curve and given the expected exponential signal attenuation of equation (50). Note the correlation of the two captured signals' deviance from the theoretical curves for a given value of τ_{21} . We attribute this to the laser system's power fluctuation on the time scale between data captures as τ_{21} was varied.

Experiment III: 6WMM with 5-Bit Bi-Phase Barker Codes

It is possible to quantify the phase-conjugate nature of the coherence-state pathways by introducing temporally complex, asymmetric waveforms. If pulse 1 is a brief reference pulse while pulse 2 and 3 are complex waveforms, then the phase conjugate nature between the SPE and VE is expressed through temporal correlation and convolution. This is seen by rewriting equation (38) in terms of correlation and convolution integrals.

$$\rho^{(3)}(t) \propto [[E_1(t) \otimes E_2(t)] * E_3(t - t_{SPE}) + [E_1(t) \otimes E_2(t)] \otimes E_3(t - t_{VC})] \quad (52)$$

Here, * and \otimes represent temporal convolution and cross-correlation respectively.

The coherence rephasing time is given by:

$$t_{SPE} = t_3 + t_2 - t_1 \quad (53)$$

$$t_{VE} = t_3 - t_2 + t_1. \quad (54)$$

The expressions in equation (52) assumes that pulse 1 is temporally symmetric ($E_1(t) = E_1(-t)$) and that pulse two and three are arbitrary waveforms. The second term

of equation (52) is the coherence pathway responsible for the ‘virtual’ echo. As shown in equation (54), the VE has rephasing character at τ_{21} before pulse three. The difference in the two terms of equation (52) is now clearly distinguishable. The spatial-spectral grating is represented by the cross-correlation of $E_1(t)$ with $E_2(t)$. The recall pulse, $E_3(t)$, then is either convolved (SPE) or correlated (VE) with the grating.

The optical processing character of the coherence-state, expressed by equation (52), is experimentally demonstrated by using a brief 80ns waveform for pulse 1 and a 5-bit bi-phase return-to-zero barker code (5b-bc) sequence for waveform 2. The sequence code {1,1,1, -1,1}, where the negative bit indicates a π phase shift of the waveform, is generated through the AOM. The resulting spectral interference pattern records the temporal complexity of the 5b-bc. Choosing pulse 3 to be the same 5b-bc then exploits the high auto-correlation to side-lobe ratio of the barker code as 25 to 1 for the VE and a peak intensity ratio of 9:4:1 for the SPE²².

Six wave-mixing using the 5b-bc is depicted in Figure 3.9. The 4WM signals that pulse 4 participates in are not depicted. The experimental capture of six-wave mixing is shown on Figure 3.10 and contains the 4WM signals SPE(E1, E2, E4) and PE (E3, E4) which attempt to be replicas of the 5b-bc.

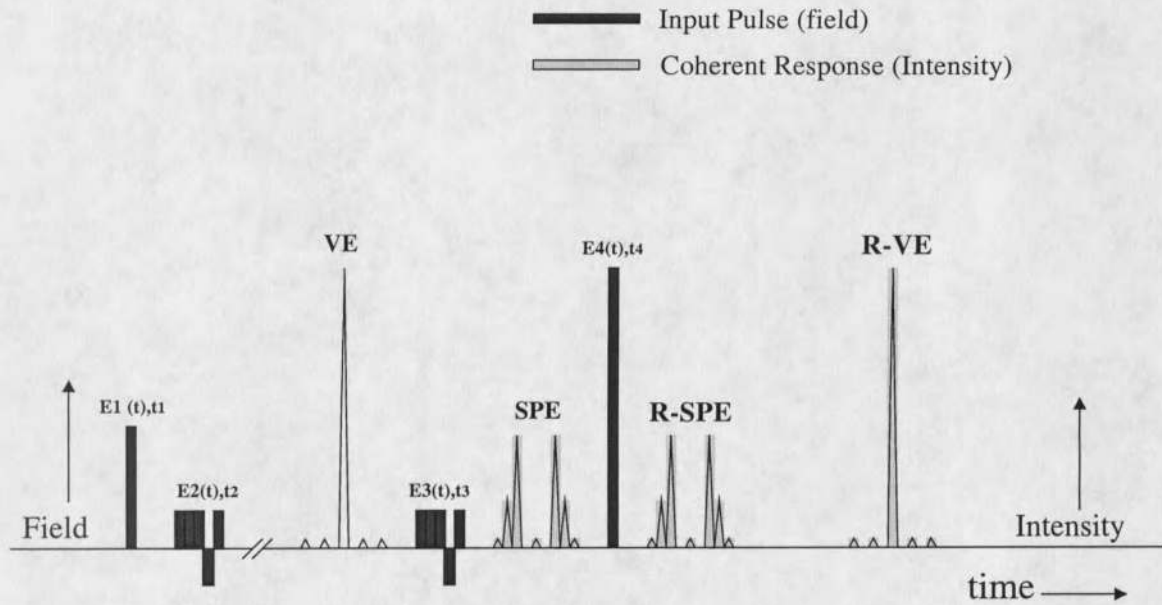


Figure 3.9: Six-wave mixing with the 5b-bc (4WM signals ignored).

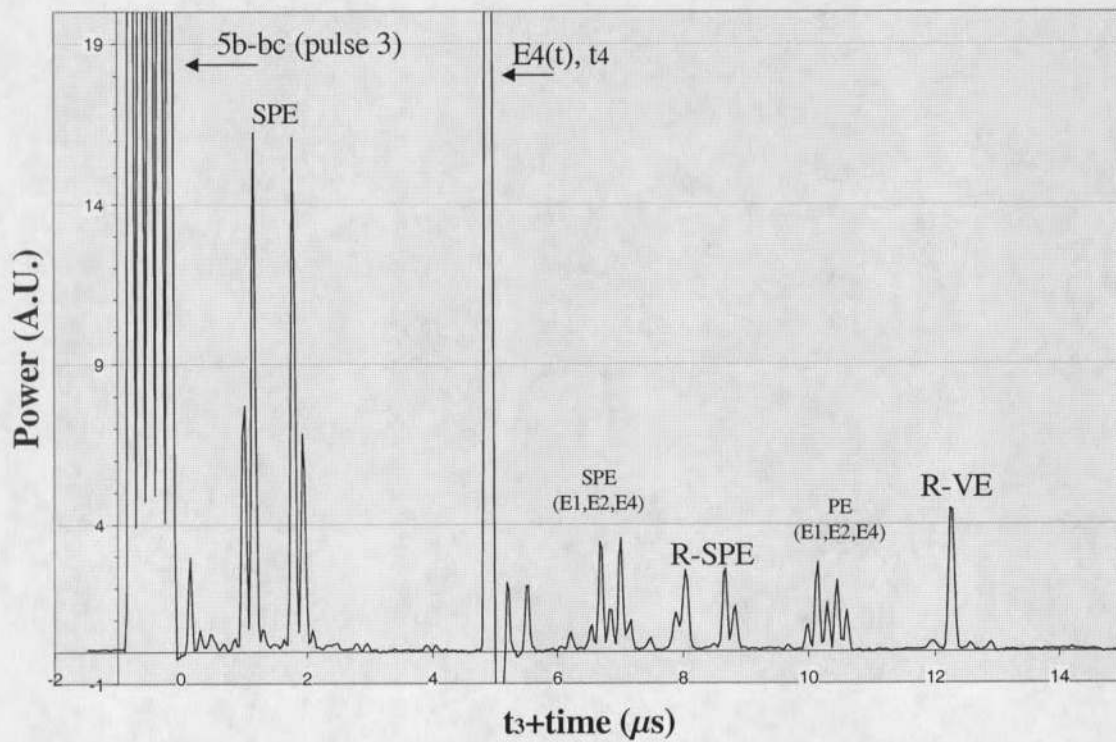


Figure 3.10: Captured signals of 6WM with 5b-bc.

CHAPTER 4

SUMMARY

The conjugate coherence-state pathways of time-domain four-wave mixing were characterized through six-wave mixing echo experiments. The time ordered echoes were verified to be six-wave mixing signals through an attenuation of θ_4 , resulting in an attenuation of the 6WM signal intensity. The coherence-state pathways were related to a common temporal origin through their mutual coherence decay. The phase conjugate nature of the paths was established through optical processing of a complex waveforms, resulting in the output signals representing an auto-correlation and auto-convolution of the complex waveform.

This work verifies that as τ_{21} is increased from zero, the phase conjugate symmetry, found in the electric fields of classical holography, is retained in the coherence-state pathways of frequency holography.

Further studies on the relation between the conjugate coherence-state paths of 4WM could explore the response of one when the other is being interfered with by another waveform. For example, let $t_4 < t_{spe}$ and note the effects on the R-VE, or let $t_4 = t_{spe}$ and frequency chirp pulse 4, noting the effects on the R-VE.

REFERENCES CITED

1. *Persistent Spectral Hole-Burning: Science and Applications*, Vol 44 Topics in Current Physics, Edited by W. E. Moerner, (Springer, 1988).
2. T. W. Mossberg, *Opt. Lett.* **7**, 77 (1982).
3. W. R. Babbitt and T. W. Mossber, *Opt. Comm.* **65**, 185 (1988).
4. M. Mitsunaga, R. Yano, and N. Uesugi, *Opt. Lett.* **16**, 1890 (1991).
5. T. W. Mossberg, *Opt. Lett.* **17**, 535 (1992).
6. X. A. Shen, and R. Kachru, *Opt. Lett.* **18**, 1967 (1993).
7. Y. S. Bai, W. R. Babbitt, N. W. Carlson, and T. W. Mossberg, *Appl. Phys. Lett.* **45**, 714 (1984); W. R. Babbitt and J. A. Bell, *Appl. Opt.* **33**, 1538 (1994).
8. K. D. Merkel and W. R. Babbitt, *Opt. Lett.* **21**, 71 (1996).
9. K. D. Merkel and W. R. Babbitt, *Applied Optics*, **35**, 278 (1996).
10. Arnold L. Bloom, *Phys. Rev.* **98**, 1105 (1955).
11. W. P. de Boeij, M. S. Pshenichnoikov, D. A. Wiersma, *Chem. Phys.* **233**, 287 (1998).
12. P. Ye, Y. R. Shen, *Phys. Rev. A.* **25**, 2183 (1981).
13. S. G. Lipson, H. Lipson, and D. S. Tannhauser, *Optical Physics*, (Cambridge University Press 1969).
14. H. Schwoerer, D. Erni, and A. Rebane, *J. Opt. Soc. Am. B*, **12**, 1083 (1995).
15. M. Mitsunaga and R. G. Brewer, *Phys. Rev. A*, **32**, 1605 (1985); K. Duppen and D. A. Wiersma, *J. Opt. Soc. Am. B*, **3**, 614 (1986).
16. S. Mukamel, *Principles of Nonlinear Optical Spectroscopy*, (Oxford Univ. Press. 1995).

17. J. J. Sakurai, *Modern Quantum Mechanics*, (Addison Wesley. 1994).
18. C. Cohen-Tannoudji, B. Diu and F. Laloe, *Quantum Mechanics*, Vol. 1 (John Wiley and Sons 1977).
19. C. S. Cornish (to be published in *Phys. Rev. A*).
20. R. N. Bracewell, *The Fourier Transform and Its Applications*, (McGraw-Hill, 1986).
21. Y. Sun (to be published in *Phys. Rev. B*).
22. S. W. Golomb and R. A. Scholtz, *IEEE Transaction on Information Theory*, Vol. IT-11, 4, 533 (1965).

MONTANA STATE UNIVERSITY - BOZEMAN



3 1762 10331181 5